CP-violation in the two Higgs doublet model: From the LHC to EDMs

Chien-Yi Chen*
Department of Physics and Astronomy, University of Victoria, Victoria, British Columbia V8P 5C2, Canada, and Perimeter Institute for Theoretical Physics, Waterloo, Ontario N2L 2Y5, Canada

Hao-Lin Li†
Amherst Center for Fundamental Interaction Department of Physics, University of Massachusetts-Amherst, Amherst, Massachusetts 01003, USA

Michael Ramsey-Musolf‡
Amherst Center for Fundamental Interaction Department of Physics, University of Massachusetts-Amherst, Amherst, Massachusetts 01003, USA, and Kellogg Radiation Laboratory, California Institute of Technology, Pasadena, California 91125, USA

(Received 27 September 2017; published 29 January 2018)

We study the prospective sensitivity to *CP*-violating two Higgs doublet models from the 14 TeV LHC and future electric dipole moment (EDM) experiments. We concentrate on the search for a resonant heavy Higgs that decays to a Z boson and a SM-like Higgs h, leading to the $Z(\ell\ell)h(b\bar{b})$ final state. The prospective LHC reach is analyzed using the Boosted Decision Tree method. We illustrate the complementarity between the LHC and low energy EDM measurements and study the dependence of the physics reach on the degree of deviation from the alignment limit. In all cases, we find that there exists a large part of parameter space that is sensitive to both EDMs and LHC searches.

DOI: 10.1103/PhysRevD.97.015020

I. INTRODUCTION

With the discovery of the Higgs-like boson at the LHC [1,2], the remaining particle predicted by the Standard Model (SM) has been found. Up to now, the measured properties of this new resonance show no significant deviation from the SM predictions. Nevertheless, the new boson could reside in a larger structure with an extended scalar sector that incorporates the SM. The possibilities for such extended scalar sectors abound. Among the most widely considered and theoretically well-motivated are two Higgs doublet models (2HDMs). Even with the rather minimal introduction of a second $SU(2)_L$ scalar doublet, the possible phenomenological consequences of 2HDMs are rich and diverse. The possibility of new sources of *CP*-violation is one of the most interesting but, perhaps, less extensively studied.

Explaining the cosmic matter and antimatter asymmetry requires the existence of additional *CP*-violation (CPV) beyond that of the SM. Electroweak baryogenesis (EWBG) is one of the most compelling solutions to this problem [3–5]. EWBG fulfills the Sakharov conditions for successful baryogenesis [6] (B violation, out-of-equilibrium dynamics, and both C and *CP*-violation) through $B+L$ violating sphaleron transitions, a strong first order electroweak phase transition that proceeds through bubble nucleation, and CPV interactions at the bubble wall. While the SM would in principle provide these ingredients, it is known that the CPV effects generated by the Cabibbo-Kobayashi-Maskawa matrix and QCD θ term are too feeble and that the SM-like Higgs scalar is too heavy for a strongly first order electroweak phase transition [7–9].

The 2HDMs provide possible solutions to these shortcomings. The viability of a strong first order electroweak phase transition and the favored parameter space of the 2HDMs have been studied in Refs. [10–12]. In the CPV sector, the LHC has already excluded the new boson as a pure *CP* odd scalar at 99.98% CL and 97.8% CL in Ref. [13] and Ref. [14], respectively.

If the boson is a part of the 2HDM, it could nevertheless receive a small *CP*-odd admixture from *CP*-violating terms in the scalar potential. This possibility for 2HDM *CP*-violation is strongly bounded by the nonobservation of

*cchen@perimeterinstitute.ca
†haolinli@physics.umass.edu
‡mjrm@physics.umass.edu

permanent electric dipole moments (EDMs) of the neutron, electron, and diamagnetic atoms, including mercury and radium [15–18], as analyzed recently in Refs. [19–23]. The authors of Refs. [24–28] also pointed out that LHC searches for additional, heavy scalars can be complementary to EDM searches, especially in regions of 2HDM parameter space where strong cancellations between Barr-Zee EDM diagrams occur. Nonetheless, there exists a window for sufficient CPV to generate the matter-antimatter asymmetry, as shown in Ref. [29].

In what follows, we analyze the prospects for future LHC probes of the CPV 2HDM, building on the previous studies in Ref. [19] and Ref. [24], where EDMs constraints and 8 TeV LHC results in CPV 2HDMs are analyzed in detail. We adopt the framework of CPV 2HDMs with a softly broken Z_2 symmetry to avoid a problematic tree level flavor changing neutral currents (FCNCs). We consider future LHC searches for a heavy Higgs of mixed CP (denoted $h_{i=2,3}$) which decays to a Z boson and a SM-like Higgs (h_1), and obtain the prospective reach for Run II and the high luminosity phase (HL-LHC). We concentrate on the $llb\bar{b}$ final state, where the Z boson decays to a pair of leptons (e or μ), and the SM-like Higgs decays to a pair of b quarks, because it is one of the most sensitive channels and because the final state particles allow for a relatively high reconstruction efficiency. We first follow the cut-based analysis procedure described in Ref. [30] to reproduce the ATLAS 8 TeV results and validate our Monte Carlo signal and background generation, then use the Boosted Decision Tree (BDT) [31] method to obtain the 95% CLs exclusion limit for future 14 TeV experiments with integrated luminosities equal to 300 fb^{-1}, and 3000 fb^{-1}, respectively. We subsequently translate the prospective exclusion limits into constraints on the parameter space, and find that a large portion of parameter space can be tested with both future LHC and EDMs experiments.

From the global fit of Higgs coupling measurements [32,33], one finds that the current data favor the 2HDMs to be close to the alignment limit: $\beta - \alpha = \pi/2$, where α and β are defined in Sec. II B and Sec. II A, respectively. Therefore, we summarize our finding in the following two categories with the combined analysis of the future EDMs and LHC exclusion bounds shown in Figs. 7 and 8.

(i) 2HDMs in alignment limit: With a discovery at the future LHC, the Type-I 2HDM would imply observation of nonzero radium and electron EDMs in the next generation searches, while the Type-II 2HDM would imply nonzero neutron and radium EDMs. A null result at the future LHC will still allow for the CPV 2HDMs if the CPV effect in the model is sufficiently small. Future EDM may still yield nonvanishing results in this case.

(ii) 2HDMs away from the alignment limit: With a discovery at the future LHC, one may or may not expect nonzero EDM results depending on the level of deviation. This is due to the fact that the production of the mostly CP odd Higgs in the model (h_3 defined in Sec. II B) is sensitive to the deviation from the alignment limit which is not suppressed by a small CPV effect. As a result, the discovery at LHC may indicate a relatively large deviation from the alignment limit instead of a large CPV effect. A null result at future LHC may not exclude the CPV 2HDMs if the CPV effect and the deviation from the alignment limit are sufficiently small. For a relatively large deviation from the alignment limit, any nonzero EDM results would disfavor the CPV 2HDMs.

The above conclusions are based on the detailed analysis discussed in Sec. V.

We also point out that our analysis will break down in some regions of parameter space that have both small values of $\tan\beta$ (ratio of the vacuum expectation values of the two neutral scalars) and the CPV Higgs mixing angle α_b, where the interference between the resonant amplitude ($gg \to h_{2,3} \to Zh_1$) and nonresonant amplitude (box diagram $gg \to Zh_1$) for Zh_1 production may become significant. We do not perform a full analysis of this effect, but rather give a qualitative estimate, as this region does not appear to significantly impact the prospective Run II exclusion reach.

The organization of our paper is the following. In Sec. II, we describe our setup for CP-violation 2HDMs. In Sec. III, we show the analytical formulas used to derive constraints on the parameter space. In Sec. IV we describe details of our simulation and analyses. In Sec. V, we exhibit future LHC constraints and discuss possible issues arising from the interference between the resonant and nonresonant diagrams. Finally, we conclude in Sec. VI. The distributions of kinematic variables used in BDT analysis are listed in Figs. 11–14 of Appendix A. The formulas for two-body decay rates of heavy Higgses are given in Appendix B.

II. CPV 2HDM MODEL DESCRIPTION

In this section, we describe details of the CPV 2HDM framework that will be used in the following discussions.

A. General 2HDM scalar potential

The most general 2HDM scalar potential containing two Higgs doublets ϕ_1 and ϕ_2 can be expressed in the following form:

$$V(\phi_1,\phi_2) = -\frac{1}{2}[m_{11}^2(\phi_1^\dagger\phi_1) + (m_{12}^2(\phi_1^\dagger\phi_2) + \text{H.c.}) + m_{22}^2(\phi_2^\dagger\phi_2)] + \frac{\lambda_1}{2}(\phi_1^\dagger\phi_1)^2 + \frac{\lambda_2}{2}(\phi_2^\dagger\phi_2)^2 + \lambda_3(\phi_1^\dagger\phi_1)(\phi_2^\dagger\phi_2) + \lambda_4(\phi_1^\dagger\phi_2)(\phi_2^\dagger\phi_1) + \frac{1}{2}[\lambda_5(\phi_1^\dagger\phi_2)^2 + \lambda_6(\phi_1^\dagger\phi_2)(\phi_1^\dagger\phi_1) + \lambda_7(\phi_1^\dagger\phi_2)(\phi_2^\dagger\phi_2) + \text{H.c.}]. \quad (1)$$

Two fields ϕ_1 and ϕ_2 can be expressed as

$$\phi_1 = \begin{pmatrix} H_1^+ \\ \frac{1}{\sqrt{2}}(v_1 + H_1^0 + iA_1^0) \end{pmatrix},$$
$$\phi_2 = \begin{pmatrix} H_2^+ \\ \frac{1}{\sqrt{2}}(v_2 + H_2^0 + iA_2^0) \end{pmatrix}, \tag{2}$$

where v_1 and v_2 are in general complex and $v = \sqrt{|v_1|^2 + |v_2|^2} = 246$ GeV. We also denote that $\tan\beta = |v_2|/|v_1|$. One can always perform a $SU(2)_L \times U(1)_Y$ gauge transformation to go into a basis where v_1 is real while $v_2 = |v_2|e^{i\xi}$ is still complex.

To guarantee that there are no FCNCs at tree level, one can assign Z_2 charges to the two Higgs doublets as well as the fermion fields such that each fermion can only couple to one of the Higgs doublets. Depending on the transformation of the fermion fields under the Z_2 symmetry, there can be various types of 2HDMs that we will introduce in Sec. II C. The Z_2 symmetry implies the potential parameters m_{12}^2 and $\lambda_{6,7}$ vanish, which in turn forbids the presence of *CP* phases in the potential. Therefore, we retain the m_{12}^2 term which only softly breaks the Z_2 symmetry. In general, this soft Z_2 symmetry breaking term together with quartic Z_2 conserving term would induce new quartic Z_2 breaking terms by renormalization, but they are at one-loop level and thus do not induce new FCNC at tree level.

Hermicity implies that there are only two complex parameters, m_{12}^2 and λ_5, in the potential. With the global phase redefinition of the fields $\phi_j \to e^{i\theta_j}\phi_j$, one may define two rephasing invariant phases as in Ref [19],

$$\delta_1 = \mathrm{Arg}[\lambda_5^*(m_{12}^2)^2], \tag{3}$$

$$\delta_2 = \mathrm{Arg}[\lambda_5^*(m_{12}^2)v_1 v_2^*]. \tag{4}$$

The minimization of the potential yields that:

$$\begin{aligned} m_{11}^2 &= \lambda_1 v^2\cos^2\beta + (\lambda_3+\lambda_4)v^2\sin^2\beta - \mathrm{Re}(m_{12}^2 e^{i\xi})\tan\beta \\ &\quad + \mathrm{Re}(\lambda_5 e^{2i\xi})v^2\sin^2\beta, \\ m_{22}^2 &= \lambda_2 v^2\sin^2\beta + (\lambda_3+\lambda_4)v^2\cos^2\beta - \mathrm{Re}(m_{12}^2 e^{i\xi})\cot\beta \\ &\quad + \mathrm{Re}(\lambda_5 e^{2i\xi})v^2\cos^2\beta, \end{aligned} \tag{5}$$

$$\mathrm{Im}(m_{12}^2 e^{i\xi}) = v^2\sin\beta\cos\beta\mathrm{Im}(\lambda_5 e^{2i\xi}). \tag{6}$$

Eq. (6) above indicates that the value of ξ is determined by given m_{12}^2 and λ_5. Expressing this equation with rephasing invariant phases implies:

$$|m_{12}^2|\sin(\delta_2 - \delta_1) = |\lambda_5 v_1 v_2|\sin(2\delta_2 - \delta_1). \tag{7}$$

In short, there is only one *CP*-independent phase in the potential after electroweak symmetry breaking (EWSB). Using this rephasing freedom of the fields, we will work in a basis where $\xi = 0$ and encode this invariant CPV phase into a CPV angle in the diagonalization matrix for the neutral Higgs sector.

B. Higgs mass eigenstates

After EWSB, we can use the following relations to diagonalize the mass matrix for the charged Higgs sector, which separates the physical charged Higgs and would-be Goldstone bosons:

$$\begin{pmatrix} H^+ \\ G^+ \end{pmatrix} = \begin{pmatrix} -s_\beta & c_\beta \\ c_\beta & s_\beta \end{pmatrix}\begin{pmatrix} {H_1}^+ \\ {H_2}^+ \end{pmatrix}. \tag{8}$$

This leads to a relationship between the mass of the charged Higgs and parameters in the scalar potential:

$$\begin{aligned} m_{H^+}^2 &= \frac{1}{2}(2\nu - \lambda_4 - \mathrm{Re}\lambda_5)v^2, \\ \nu &\equiv \frac{\mathrm{Re}m_{12}^2\csc\beta\sec\beta}{2v^2}, \end{aligned} \tag{9}$$

where the parameter ν sets the hierarchy between the SM-like Higgs and charged Higgs. The mass term in the Lagrangian is given by $\mathcal{L}_{\mathrm{neutral}}^{\mathrm{mass}} = -(H_1^0, H_2^0, A^0)\mathcal{M}^2(H_1^0, H_2^0, A^0)^T$ gives,

$$\mathcal{M}^2 = v^2\begin{pmatrix} \lambda_1 c_\beta^2 + \nu s_\beta^2 & (\lambda_{345} - \nu)c_\beta s_\beta & -\frac{1}{2}\mathrm{Im}\lambda_5 s_\beta \\ (\lambda_{345} - \nu)c_\beta s_\beta & \lambda_2 s_\beta^2 + \nu c_\beta^2 & -\frac{1}{2}\mathrm{Im}\lambda_5 c_\beta \\ -\frac{1}{2}\mathrm{Im}\lambda_5 s_\beta & -\frac{1}{2}\mathrm{Im}\lambda_5 c_\beta & -\mathrm{Re}\lambda_5 + \nu \end{pmatrix}, \tag{10}$$

where λ_{345} represents $\lambda_3 + \lambda_4 + \mathrm{Re}(\lambda_5)$. A rotation matrix R defined below can be used to diagonalize the mass matrix:

$$R = \begin{pmatrix} -s_\alpha c_{\alpha_b} & c_\alpha c_{\alpha_b} & s_{\alpha_b} \\ s_\alpha s_{\alpha_b} s_{\alpha_c} - c_\alpha c_{\alpha_c} & -s_\alpha c_{\alpha_c} - c_\alpha s_{\alpha_b} s_{\alpha_c} & c_{\alpha_b} s_{\alpha_c} \\ s_\alpha s_{\alpha_b} c_{\alpha_c} + c_\alpha s_{\alpha_c} & s_\alpha s_{\alpha_c} - c_\alpha s_{\alpha_b} c_{\alpha_c} & c_{\alpha_b} c_{\alpha_c} \end{pmatrix}, \tag{11}$$

where s_α and c_α are short hands for $\sin\alpha$ and $\cos\alpha$. Under this rotation matrix, we have $\mathcal{M}^2 = R^T\mathrm{diag}(m_{h_1}^2, m_{h_2}^2, m_{h_3}^2)R$, and $R(H_1^0, H_2^0, A^0)^T = (h_1, h_2, h_3)^T$. We demand that three rotation angles are in the following range:

$$-\frac{\pi}{2} < \alpha, \alpha_b, \alpha_c < \frac{\pi}{2}. \tag{12}$$

With this diagonalization procedure, one can obtain six linearly independent equations which can be solved for the parameters in the scalar potential in terms of the physical parameters, as shown below [19],

$$\lambda_1 = \frac{m_{h_1}^2 \sin^2\alpha \cos^2\alpha_b + m_{h_2}^2 R_{21}^2 + m_{h_3}^2 R_{31}^2}{v^2 \cos\beta^2} - \nu \tan^2\beta, \tag{13}$$

$$\lambda_2 = \frac{m_{h_1}^2 \cos^2\alpha \cos^2\alpha_b + m_{h_2}^2 R_{22}^2 + m_{h_3}^2 R_{32}^2}{v^2 \sin\beta^2} - \nu \cot^2\beta, \tag{14}$$

$$\mathrm{Re}\lambda_5 = \nu - \frac{m_{h_1}^2 \sin^2\alpha_b + \cos^2\alpha_b (m_{h_2}^2 \sin^2\alpha_c + m_{h_3}^2 \cos^2\alpha_c)}{v^2}, \tag{15}$$

$$\lambda_3 = \nu - \frac{m_{h_1}^2 \sin\alpha \cos\alpha \cos^2\alpha_b - m_{h_2}^2 R_{21} R_{22} - m_{h_3}^2 R_{31} R_{32}}{v^2 \sin\beta \cos\beta} - \lambda_4 - \mathrm{Re}\lambda_5, \tag{16}$$

$$\mathrm{Im}\lambda_5 = \frac{2\cos\alpha_b [(m_{h_2}^2 - m_{h_3}^2)\cos\alpha \sin\alpha_c \cos\alpha_c + (m_{h_1}^2 - m_{h_2}^2 \sin^2\alpha_c - m_{h_3}^2 \cos^2\alpha_c)^2 \sin\alpha \sin\alpha_b]}{v^2 \sin\beta}, \tag{17}$$

$$\tan\beta = \frac{(m_{h_2}^2 - m_{h_3}^2)\cos\alpha_c \sin\alpha_c + (m_{h_1}^2 - m_{h_2}^2 \sin^2\alpha_c - m_{h_3}^2 \cos^2\alpha_c)\tan\alpha \sin\alpha_b}{(m_{h_2}^2 - m_{h_3}^2)\tan\alpha \cos\alpha_c \sin\alpha_c - (m_{h_1}^2 - m_{h_2}^2 \sin^2\alpha_c - m_{h_3}^2 \cos^2\alpha_c)\sin\alpha_b}. \tag{18}$$

The last equation relates the two CPV angles, α_c and α_b, and indicates that there exists only one independent CPV phase in our model. Using Eq. (9) and the minimization condition Eq. (5) we obtain the full relationships between model parameters (λ_1, λ_2, λ_3, λ_4, $\mathrm{Re}\lambda_5$, $\mathrm{Im}\lambda_5$, m_{11}^2, m_{22}^2, $\mathrm{Re}m_{12}^2$, $\mathrm{Im}m_{12}^2$) and phenomenological parameters (v, $\tan\beta$, ν, α, α_b, α_c, m_{h_1}, m_{h_2}, m_{h_3}, m_{H^+}). Through Eq. (18), one can solve for the angle α_b in terms of α_c,

$$\alpha_b = -\arcsin\left[\frac{(m_{h_2}^2 - m_{h_3}^2)\sin 2\alpha_c \cot(\beta+\alpha)}{2(m_{h_1}^2 - m_{h_2}^2 \sin^2\alpha_c - m_{h_3}^2 \cos^2\alpha_c)}\right]. \tag{19}$$

Conversely, one could obtain the formula for α_c in terms of α_b. However, two solutions will be generated when solving the second order equation for $\tan\alpha_c$. Here we adopt the convention in Ref. [24],

$$\alpha_c = \begin{cases} \alpha_c^-, & \alpha+\beta \le 0 \\ \alpha_c^+, & \alpha+\beta > 0 \end{cases},$$

$$\tan\alpha_c^{\pm} = \frac{\mp|\sin\alpha_b^{\max}| \pm \sqrt{\sin^2\alpha_b^{\max} - \sin^2\alpha_b}}{\sin\alpha_b} \sqrt{\frac{m_{h_3}^2 - m_{h_1}^2}{m_{h_2}^2 - m_{h_1}^2}}, \tag{20}$$

where $\sin\alpha_b^{\max}$ sets a theoretical bound on the CPV angle α_b which comes from the requirement of the existence of a real solution for $\tan\alpha_c$:

$$\sin^2\alpha_b \le \frac{(m_{h_3}^2 - m_{h_2}^2)^2 \cot^2(\alpha+\beta)}{4(m_{h_2}^2 - m_{h_1}^2)(m_{h_3}^2 - m_{h_1}^2)} \equiv \sin^2\alpha_b^{\max}. \tag{21}$$

C. Interaction terms

To eliminate the tree level FCNCs, one can assign Z_2 charges to different fermion fields. In general, this would lead to four possible arrangements in the Yukawa sector, which are often dubbed Type-I, Type-II, Lepton-specific and Flipped 2HDMs [34–36]. In this work, we only concentrate on the first two, since Type-I (Type-II) differs from Lepton-specific (Flipped) only in the lepton sector and they should behave similarly to the first two in our collider and EDMs experiments. Under the Z_2 symmetry fermion fields transform as

$$Q_L \to Q_L \qquad u_R \to u_R \qquad d_R \to d_R, \qquad \text{Type I}, \tag{22}$$

$$Q_L \to Q_L \qquad u_R \to u_R \qquad d_R \to -d_R, \qquad \text{Type II}. \tag{23}$$

The corresponding Yukawa interactions invariant under the Z_2 symmetry are:

$$\mathcal{L}_{\mathrm{I}} = -Y_U \bar{Q}_L (i\tau_2)\phi_2^* u_R - Y_D \bar{Q}_L \phi_2 d_R + \mathrm{H.c.}, \tag{24}$$

$$\mathcal{L}_{\mathrm{II}} = -Y_U \bar{Q}_L (i\tau_2)\phi_2^* u_R - Y_D \bar{Q}_L \phi_1 d_R + \mathrm{H.c.} \tag{25}$$

The interaction of the physical Higgs with fermions and with vector bosons can be parametrized as

$$\mathcal{L}_{\mathrm{int}} = -\frac{m_f}{v} h_i (c_{f,i} \bar{f} f + \tilde{c}_{f,i} \bar{f} i\gamma_5 f) + a_i h_i \left(\frac{2m_W^2}{v} W_\mu W^\mu + \frac{m_Z^2}{v} Z_\mu Z^\mu\right), \tag{26}$$

where $c_{f,i}(\tilde{c}_{f,i})$ represents the scalar (pseudoscalar) component of the physical Higgs h_i coupling to fermions while

TABLE I. Couplings to Higgs mass eigenstates.

	$c_{t,i}$	$c_{b,i} = c_{\tau,i}$	$\tilde{c}_{t,i}$	$\tilde{c}_{b,i} = \tilde{c}_{\tau,i}$	a_i
Type I	$R_{i2}/\sin\beta$	$R_{i2}/\sin\beta$	$-R_{i3}\cot\beta$	$R_{i3}\cot\beta$	$R_{i2}\sin\beta + R_{i1}\cos\beta$
Type II	$R_{i2}/\sin\beta$	$R_{i1}/\cos\beta$	$-R_{i3}\cot\beta$	$-R_{i3}\tan\beta$	$R_{i2}\sin\beta + R_{i1}\cos\beta$

a_i stands for the coefficient of h_i coupling to the vector bosons. Analytic expressions for these coefficients are given in terms of the phenomenological parameters in Table I. Higgs global fits to the *CP* conserving 2HDM from current LHC measurements indicate that the couplings are close to the alignment limit: $\beta - \alpha = \pi/2$ [32,33].

Hence, we concentrate on the region having only small deviations from this limit in our study. The interaction between the heavy Higgses, SM Higgs and Z bosons can be parametrized in the following form:

$$\mathcal{L}_{h_i \to Z h_1} = g_{iz1} Z^\mu (\partial_\mu h_i h_1 - h_i \partial_\mu h_1), \tag{27}$$

with the coefficient g_{iz1} expressed as:

$$g_{iz1} = \frac{e}{\sin 2\theta_W}[(-\sin\beta R_{11} + \cos\beta R_{12}) R_{i3} - (-\sin\beta R_{i1} + \cos\beta R_{i2}) R_{13}]. \tag{28}$$

We parametrize the deviation from the alignment limit by a small variable θ where $\beta - \alpha = \pi/2 + \theta$. Then we expand coupling g_{iz1} in the limits of small α_b (CPV angle) and θ, which gives,

$$g_{2z1} \propto -\alpha_b + O(\alpha_b \theta) \tag{29}$$

$$g_{3z1} \propto -\theta + O(\alpha_b^2). \tag{30}$$

Thus, near the alignment limit, the decay $h_2 \to Z h_1$ could occur only if $\alpha_b \neq 0$, assuming it is kinematically allowed. In contrast, the decay $h_3 \to Z h_1$ could arise even in the $\alpha_b = 0$ limit so long as there exists a departure from exact alignment. Consequently, one may interpret null results of any search for a heavy scalar decaying to a Z-boson and a SM-like Higgs boson in terms of constraints on either α_b or θ. In what follows we will, thus, consider the present and prospective constraints on α_b in two cases: $\theta = 0$ and $\theta \neq 0$.

III. PRODUCTION AND DECAY OF HEAVY HIGGS

A. Production of heavy Higgs

At the LHC, the dominant production mode for a heavy Higgs is via gluon fusion. Therefore, we restrict our study on this specific production mode. The one loop gluon fusion production cross section of a heavy Higgs is obtained by rescaling the value of the production cross section for the SM-like Higgs:

$$\sigma(gg \to h_i) = \sigma(gg \to H_{\rm SM}) \frac{|c_{t,i} F^H_{1/2}(\tau^i_t) + c_{b,i} F^H_{1/2}(\tau^i_b)|^2 + |\tilde{c}_{t,i} F^A_{1/2}(\tau^i_t) + \tilde{c}_{b,i} F^A_{1/2}(\tau^i_b)|^2}{|F^H_{1/2}(\tau^i_t) + F^H_{1/2}(\tau^i_b)|^2}, \tag{31}$$

with $\tau^i_f = m^2_{h_i}/(4m^2_f)$, the ratio of the mass squared of the heavy Higgs (h_i) to 4 times the mass squared of the fermion running in the loop. Here, $\sigma(gg \to H_{\rm SM})$ represents the gluon fusion production cross section of a heavy Higgs with SM couplings. The functions $F^H_{1/2}$ and $F^A_{1/2}$ are defined in the following:

$$F^H_{1/2}(\tau) = 2(\tau + (\tau - 1) f(\tau))\tau^{-2}, \tag{32}$$

$$F^A_{1/2}(\tau) = 2 f(\tau) \tau^{-1}, \tag{33}$$

$$f(\tau) = \begin{cases} \arcsin^2(\sqrt{\tau}), & \tau \leq 1 \\ \frac{1}{4}\left[\log\left(\frac{1+\sqrt{1-\tau^{-1}}}{1-\sqrt{1-\tau^{-1}}}\right) - i\pi\right]^2, & \tau > 1 \end{cases}. \tag{34}$$

As one can see from Eq. (31), the numerator involves the sum of two contributions arising from the *CP*-odd and *CP*-even components of the physical Higgs boson, respectively. Denoting $\mathcal{M}^{gg\to h_i}_{CP-\rm odd}$ and $\mathcal{M}^{*gg\to h_i}_{CP-\rm even}$ as the *CP*-odd and *CP*-even parts of the gluon fusion matrix elements, we see that the interference term $\mathcal{M}^{gg\to h_i}_{CP-\rm odd}\mathcal{M}^{*gg\to h_i}_{CP-\rm even}$ vanishes after integrating over final state phase space due to parity. The heavy Higgs production cross section in this form automatically takes into account the K-factor, if one uses the production $\sigma(gg \to H_{\rm SM})$ with higher order corrections. Here we obtain the values of $\sigma(gg \to H_{\rm SM})$ from the Web site [37].

B. Decay of heavy Higgs

The dominant two-body decay modes of the heavy Higgses are taken into account with $\Gamma_{\rm tot}$ expressed in the following form:

$$\Gamma_{\rm tot}(h_i) = \Gamma(h_i \to gg) + \Gamma(h_i \to Zh_1) + \Gamma(h_i \to W^+W^-) + \Gamma(h_i \to ZZ) + \Gamma(h_i \to t\bar{t}) + \Gamma(h_i \to b\bar{b}) + \Gamma(h_i \to \tau^+\tau^-) + \Gamma(h_i \to h_1h_1) + \cdots, \quad (35)$$

where the "$+\cdots$ denote the tiny decay rates to a pair of light fermions and photons, and Z boson and photon, which we have neglected. In addition, we ignore decay rate of a heavy Higgs to one SM-like Higgs and another heavy Higgs, as well as a pair of heavy Higgses because they are forbidden by kinematics due to the mass hierarchy we choose in our benchmark model. The analytical expression for each two-body decay rate can be found in the Appendix B.

IV. SIMULATION DETAIL

In this section, we will discuss details of our collider simulation. We first reproduce the result of 8 TeV ATLAS exclusion limit on $\sigma(gg \to h_i) \times \mathrm{Br}(h_i \to Zh_1) \times \mathrm{Br}(h_1 \to b\bar{b})$ obtained by searching for a heavy Higgs $h_{i=2,3}$ decaying to $Z(\ell^+\ell^-)h_1(b\bar{b})$ [30] (As in Ref. [30] we do not include a $\mathrm{Br}(Z \to \ell^+\ell^-)$ factor because it is assumed to have the SM value.). We then use a BDT method to perform events classification and derive the projected exclusion limit for a future 14 TeV search. Events are generated by MadGraph 5 aMC@NLO [38] and then passed through PYTHIA6 [39] for parton showering. Finally Delphes3 [40] is used for fast detector simulation.

A. 8 TeV result reproduction

We use the cuts described in Ref. [30] as follows:

(i) The events must have 2 electrons or 2 opposite charged muons with $p_T^{e,\mu} > 7$ GeV and $|\eta_e|(|\eta_\mu|) < 2.5(2.7)$.

(ii) The leptons must have $p_{T,\mathrm{lead}}^{e,\mu} > 25$ GeV, and if the leptons are $\mu^+\mu^-$ pairs, then one of the μ must satisfy $|\eta_\mu| < 2.5$.

(iii) The events must have exactly 2 tagged b-jets with $p_{b,T}^{\mathrm{lead}} > 45$ GeV and $p_{b,T}^{\mathrm{sub}} > 20$ GeV.

(iv) The reconstructed invariant mass for dilepton and dijet systems should satisfy: $83 < m_{\ell\ell} < 99$ GeV and $95 < m_{bb} < 135$ GeV.

(v) $E_T^{\mathrm{miss}}/\sqrt{H_T} < 3.5\ \mathrm{GeV}^{1/2}$, where H_T is defined as the scalar sum of all jets and leptons in the events.

(vi) $p_T^Z > 0.44 \times M_{h2,3}^{\mathrm{rec}} - 106$ GeV, where $M_{h2,3}^{\mathrm{rec}}$ is the reconstructed mass of heavy Higgs.

For the detector simulation, we use the default Delphes ATLAS cards with b tagging efficiency equal to 70% as used in the ATLAS analysis [30]. In the mean time we also modify the following value to match the ATLAS analysis:

(i) The isolation conditions for leptons:
Change DeltaRMax from 0.5(default) to 0.2; change PTMin from 0.5(default) to 0.4(1) for electron(muon); change PTRatio from 0.1(default) to 0.15. These changes will increase the lepton identification in the boosted regime.

(ii) Change the ParameterR for jet-clustering(anit-kt) algorithm from 0.6 to 0.4.

For the signal process, we only take into account the gluon fusion production mode of the heavy Higgs. As for the background processes, we consider the two major backgrounds Zbb and $t\bar{t}$ as well as to subleading backgrounds SM Zh and diboson ZZ backgrounds. For all the backgrounds, we generate events with one additional jet with jet matching. The numbers of events generated and the corresponding acceptance times efficiency are given in Table II. The cross sections are normalized to the values with higher order corrections. The K-factors for Zbb, $t\bar{t}$, Zh, ZZ are calculated based on the result in Ref. [41–44]. One can observe that the $Z(\ell\ell)bb$ background is a bit larger than the ATLAS result in Table II. This may be due to the fact that ATLAS used a data-driven method to estimate the number of $Z(\ell\ell)bb$ background events, which may include some effects that our fast detector simulation cannot fully replicate. However, one can also see that these kinds of effects are at a controllable level; our simulation result agrees with ATLAS results within at most 20%

TABLE II. Summary of the 8 TeV simulation. The second column gives the cross section of each background process at 8 TeV LHC with generator level cuts. The signal distributions are normalized to 0.03 pb as suggested in Ref. [30]. The third column is the total number of events produced at 8 TeV LHC with the integrated luminosity equal to 20.3 fb^{-1}. The fourth column is the number of events left for each background after all the cuts with the integrated luminosity equal to 20.3 fb^{-1}. The fifth column gives the number of events left with the same cuts estimated by ALTAS in Ref. [30]. The last column gives the acceptance times the efficiency after all the cuts obtained by our simulation.

Backgrounds /signal	σ (pb)	$\sigma \times \int \mathcal{L}$	Simulated # of events after cuts	# of expected events in Ref. [30]	$A \times \epsilon$
$Z(\ell\ell)bb$	12.91	2.620×10^5	1,788	1443 ± 60	6.825×10^{-3}
$t(bl\nu)\bar{t}(bl\nu)$	18.12	3.678×10^5	359	317 ± 28	9.761×10^{-4}
SM$Z(\ell\ell)h(bb)$	0.02742	5.566×10^2	47	31 ± 1.8	8.443×10^{-2}
Diboson$(Z(\ell\ell)Z(bb))$	0.2122	4.308×10^3	28	30 ± 5	6.679×10^{-3}
Signal(500 GeV)	0.03	4.06×10^2	54	$\cdots$	1.332×10^{-1}

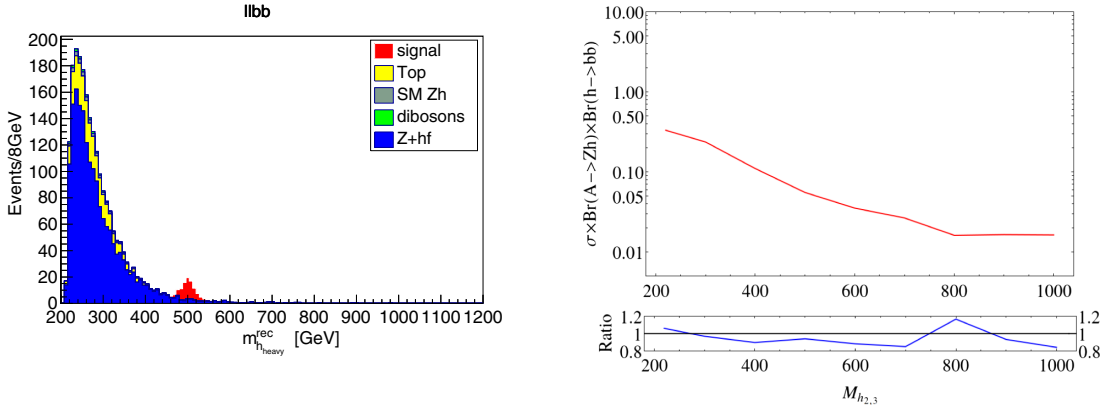

(a) $M_{h_2}^{\mathrm{rec}}$ Distribution (b) exclusion limit

FIG. 1. Fig. (a) shows the reconstructed invariant mass distributions with $\ell^+\ell^- b\bar{b}$ final state. The signal comes from a heavy Higgs of mass 500 GeV and production cross section 0.03 pb with an integrated luminosity 20.3 fb^{-1}. Fig. (b) demonstrates the 95% exclusion limit on the signal $\sigma(gg\to A)\mathrm{Br}(A\to Zh)\mathrm{Br}(h\to bb)$. The red curve is our result using the distribution in Fig. (a) with profile likelihood method while the blue curve is the ratio of the ATLAS result (in Fig. 3(b) of Ref. [30]) to our reproduced expected exclusion limit.

uncertainty. Since we may also expect the same kind of effect in 14 TeV simulations, our projected exclusion limit result will be conservative.

We present the reconstructed invariant mass of the heavy Higgs in Fig. 1(a) which can be compared with the ATLAS result in Fig. 3(b) in Ref. [30]. With this binned distribution we use a profile likelihood method as used in the ATLAS paper to reproduce the 95% CLs exclusion limit. A comparison with ATLAS result is given in Fig. 1(b), the red curve is our reproduced exclusion limit, and the blue curve is the ratio of the ATLAS results to our reproduced values. One can see that the ratio is generally less than one which corresponds to the excess of $Z(\ell\ell)bb$ background in our simulation. The peak at 800 GeV is due to the lack of background statistics and downward fluctuation near $m_{hi} = 800$ GeV, but for our benchmark models where $m_{h2} = 550$, $m_{h3} = 600$ GeV and $m_{h2} = 400$, $m_{h3} = 450$ GeV, the ratio seems reasonably close to one.

B. 14 TeV prediction

We use the same Delphes card when generating events for the 14 TeV case. The preselection cuts we use are almost the same as those for the 8 TeV case. In order to get a sufficiently large sample for BDT analysis, we expand the mass window for m_{bb} from 95–135 GeV to 60–140 GeV. Also, rather than implementing the $E_T^{\mathrm{miss}}/\sqrt{H_T}$ and p_T^Z cuts, we allow the BDT to optimize them. The numbers of events generated and the acceptance times efficiency after preselection for signal and backgrounds are given in Table III. After preselection, we use a built-in package in ROOT, Toolkit for Multivariate Data Analysis (TMVA) [45] and the BDT method for the classification of signal and background events. The variables used for the classification are listed below:

$$p_{T,\ell}^{\mathrm{lead}}, p_{T,\ell}^{\mathrm{sub}}, p_{T,b}^{\mathrm{lead}}, p_{T,b}^{\mathrm{sub}}, m_{\ell\ell}, m_{bb}, p_T^Z, p_T^h, E_T^{\mathrm{miss}}/\sqrt{H_T},$$
$$\Delta R_{\ell\ell}, \Delta R_{jj}, \Delta R_{Zh}, \Delta\phi_{Zh}, \tag{36}$$

TABLE III. Summary of the 14 TeV simulation after preselection cuts. The second column gives the cross sections for each background process after generator level cuts at the 14 TeV LHC. The signal distributions are normalized to 0.06 pb. The third column gives the number of events generated in our simulation. The fourth column shows the number of events left after the preselection cuts described in Sec. IV B before training the BDT. The last column gives the efficiency of the preselection cuts for each process.

Backgrounds /signal	σ (pb)	# of events generated	# of events remaining after cuts	Preselection efficiency
$Z(\ell\ell)bb$	36.57	7.084×10^6	94,323	1.331×10^{-2}
$t(bl\nu)\bar{t}(bl\nu)$	68.11	3.276×10^7	120,627	3.680×10^{-3}
SMZ$(\ell\ell)h(bb)$	0.0502	1.429×10^5	14,380	1.006×10^{-1}
Diboson$(Z(bb)Z(\ell\ell))$	0.3833	1.780×10^6	80,887	4.554×10^{-3}
Signal(550 GeV)	0.06	1.0×10^5	20,645	0.2065
Signal(600 GeV)	0.06	1.0×10^5	21,392	0.2139

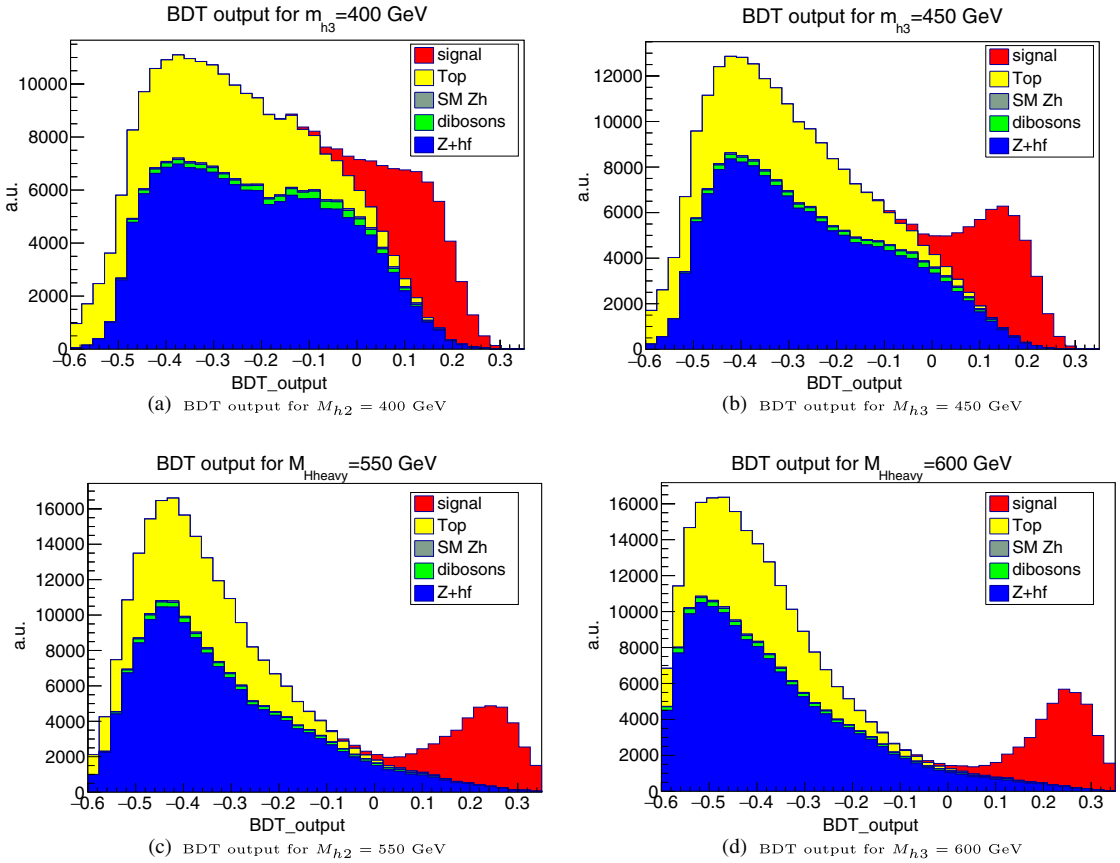

(a) BDT output for $M_{h2} = 400$ GeV (b) BDT output for $M_{h3} = 450$ GeV

(c) BDT output for $M_{h2} = 550$ GeV (d) BDT output for $M_{h3} = 600$ GeV

FIG. 2. The BDT output distributions for both signal and backgrounds. The signals in Figs. (a) and (b) are for heavy Higgses with masses 400, 450, 550 and 600 GeV, respectively. The background distributions are normalized to the actual 14 TeV cross sections in Ref. [37], while the signal distributions are normalized to 0.06 pb.

where $p_{T,(j,\ell)}^{\text{lead,sub}}$ represent the leading and subleading p_T of leptons and jets; $m_{\ell\ell}$ and m_{bb} are the invariant masses of dijet and dilepton systems, respectively; $p_T^{h,Z}$ stands for the reconstructed p_T of the Z boson and the SM Higgs; $E_T^{\text{miss}}/\sqrt{H_T}$ is the ratio of the missing transverse energy to $\sqrt{H_T}$ defined in the previous subsection; $\Delta R_{\ell\ell,bb,Zh}$ are the angular separations of two leptons, two bjets and reconstructed Zh, respectively, with $\Delta R_{ab} = \sqrt{(\eta_a - \eta_b)^2 + (\phi_a - \phi_b)^2}$. $\Delta\phi_{Zh}$ is the separation of the azimuthal angles between Z and h. The distributions of these variables are shown in Figs. 11 to 14 in Appendix A.

We select representative points with $M_{h2} = 400$, $M_{h3} = 450$, $M_{h2} = 550$ and $M_{h3} = 600$ GeV as the signal to train the BDT. The BDT algorithm settings in TMVA are:

NTrees = 850; MiniNodeSize = 2.5%; MaxDepth = 3;

BoostType = AdaBoost; AdaBoostBoostBeta = 0.5;

SeparationType = GiniIndex; nCuts = 20.

The distributions of the BDT output for two heavy Higgs masses are shown in Figs. 2(c) and 2(d). One could find that the discriminating power is a bit better for the heavier Higgs as we expected.

The next step is to select a cut on the BDT output to obtain the most stringent 95% exclusion limits. After applying the BDT cuts shown in Tables VI and VII, we use the reconstructed heavy Higgs mass distribution of the remaining events to derive the 95% exclusion limit on $\sigma(gg \to h_{2,3})\text{Br}(h_{2,3} \to Zh_1)\text{Br}(h_1 \to b\bar{b})$. We show the resulting prospective exclusion limits in Tables VI and VII. We also perform a cut-based analysis with the same ATLAS cuts described in Sec. IV A, and the results are shown in the "cut-based result" column in Tables VI and VII. One can see that the exclusion limits of our BDT analysis are 30% to 50% better (lower) than the cut-based analysis results.

V. RESULTS AND DISCUSSION

We now translate our simulated exclusion limit into constraints on the parameter space of CPV 2HDMs. We mainly focus on the benchmark point below which is consistent with the electroweak precision measurements and muon $g-2$ data as discussed in Ref. [24]:

$$m_{h_2} = 550\ \text{GeV}, \qquad m_{h_3} = 600\ \text{GeV},$$
$$m_{H^\pm} = 620\ \text{GeV}, \qquad \nu = 1 \tag{37}$$

and show the constraints on $\sin\alpha_b$ vs $\tan\beta$. As a comparison we also include the constraints in the alignment limit for a lighter mass benchmark point: $m_{h_2} = 400$ GeV, $m_{h_3} = 450$ GeV, $m_{H^\pm} = 420$ GeV, $\nu = 1$. The reason we choose a relatively small mass splitting between the two heavy Higgses is that this splitting is tightly constrained by bounds on the T parameter from electroweak precision data. The study in Ref. [24] shows that a splitting round 50 GeV is already marginally consistent with electroweak precision data.

The 95% CLs exclusion limit is given by:

$$\sigma(gg \to h_{2,3}) \times \text{Br}(h_{2,3} \to Zh_1) \times \text{Br}(h_1 \to b\bar{b}) < \sigma_L, \tag{38}$$

where σ_L are the exclusion limit for different luminosity for $m_{h2} = 400$ GeV, $m_{h2} = 450$ GeV, $m_{h2} = 550$ GeV and $m_{h3} = 600$ GeV that listed in IV, V, VI and VII respectively. We assume that the resonance process is dominant when the invariant mass of two gluons is approaching the mass of the heavy Higgs. This is not always true in the parameter space we consider, especially in the limit of small θ. The gluon fusion to Zh_1 box diagram may become important and interfere with the resonant triangle diagram. This may change the distribution of the invariant mass of Zh_1. Here, we will simply identify the region of parameter space that may suffer from this effect, leaving a detailed analysis for future study. To proceed, we will compare the relative scale of the amplitude squared of the resonant and nonresonant $gg \to Zh_1$ processes at the center of mass energy $\sqrt{s} = m_{h_2}$, and m_{h_3}. For the resonance contribution we use the following formula

$$\overline{|M_i|^2} = \frac{G_F \alpha_s^2 |g_{iz1}|^2 s^2}{512\pi^2\sqrt{2}} \left[\left| \sum_{f=t,b} c_{f,i} F_{1/2}^H(\tau_f^i) \right|^2 + \left| \sum_{f=t,b} \tilde{c}_{f,i} F_{1/2}^A(\tau_f^i) \right|^2 \right] \times \frac{M_Z^2 - 2m_{h_1}^2 - 2s + (m_{h_i}^2 - s)^2/M_Z^2}{(s - m_{h_i}^2)^2 + m_{h_i}^2 \Gamma_{h_i}^2}, \tag{39}$$

where G_F and α_s are the Fermi constant and strong coupling constant, respectively, while g_{iz1}, $F_{1/2}^{A/H}$, c_f, $\tilde{c_f}$, and Γ_{h_i} are defined in Secs. II and III. For the nonresonant piece we obtain the scale of $\overline{M_{\text{box}}^2} \simeq 10^{-5}$ from Ref. [46]. In presenting our results in Figs. 3–5, we include contours of constant $|M_i|^2$ in order to identify regions where the resonant and nonresonant contributions are commensurate in scale.

TABLE IV. Exclusion limits σ_L for $\sigma(gg \to h_2) \times \text{Br}(h_2 \to Zh_1) \times \text{Br}(h_1 \to b\bar{b})$ and best cuts on BDT output of different luminosities for $M_{h_2} = 400$ GeV. The column "Cut-based result" gives the exclusion limit derived from the ATLAS cut-based analysis described in Sec. IV A.

$M_{h_2} = 400$ GeV (14 TeV)			
Luminosity (fb^{-1})	Best cut	Exclusion limit σ_L (pb)	Cut-based result (pb)
100	0.14	0.0582	0.1003
300	0.14	0.0336	0.0571
3000	0.14	0.0103	0.0185

TABLE V. Exclusion limits σ_L for $\sigma(gg \to h_2) \times \text{Br}(h_2 \to Zh_1) \times \text{Br}(h_1 \to b\bar{b})$ and best cuts on BDT output of different luminosities for $M_{h_2} = 450$ GeV. The column "Cut-based result" gives the exclusion limit derived from the ATLAS cut-based analysis described in Sec. IV A.

$M_{h_3} = 450$ GeV (14 TeV)			
Luminosity (fb^{-1})	Best cut	Exclusion limit Fig (pb)	Cut-based result (pb)
100	0.15	0.0506	0.0700
300	0.16	0.0292	0.0571
3000	0.16	0.00901	0.0185

TABLE VI. Exclusion limits σ_L for $\sigma(gg \to h_2) \times \text{Br}(h_2 \to Zh_1) \times \text{Br}(h_1 \to b\bar{b})$ and best cuts on BDT output of different luminosities for $M_{h_2} = 550$ GeV. The column "Cut-based result" gives the exclusion limit derived from the ATLAS cut-based analysis described in Sec. IV A.

$M_{h_2} = 550$ GeV (14 TeV)			
Luminosity (fb^{-1})	Best cut	Exclusion limit σ_L (pb)	Cut-based result (pb)
100	0.22	0.0299	0.0443
300	0.22	0.0167	0.0261
3000	0.22	0.00510	0.00782

TABLE VII. Exclusion limits σ_L for $\sigma(gg \to h_3) \times \text{Br}(h_3 \to Zh_1) \times \text{Br}(h_1 \to b\bar{b})$ and best cuts on BDT output of different luminosities for $M_{h_3} = 600$ GeV. The column "Cut-based result" gives the exclusion limit derived from the ATLAS cut-based analysis described in Sec. IV A.

$M_{h_3} = 600$ GeV (14 TeV)			
Luminosity (fb^{-1})	Best cut	Exclusion limit σ_L (pb)	Cut-based result (pb)
100	0.21	0.0248	0.0340
300	0.22	0.0138	0.0192
3000	0.22	0.00423	0.00598

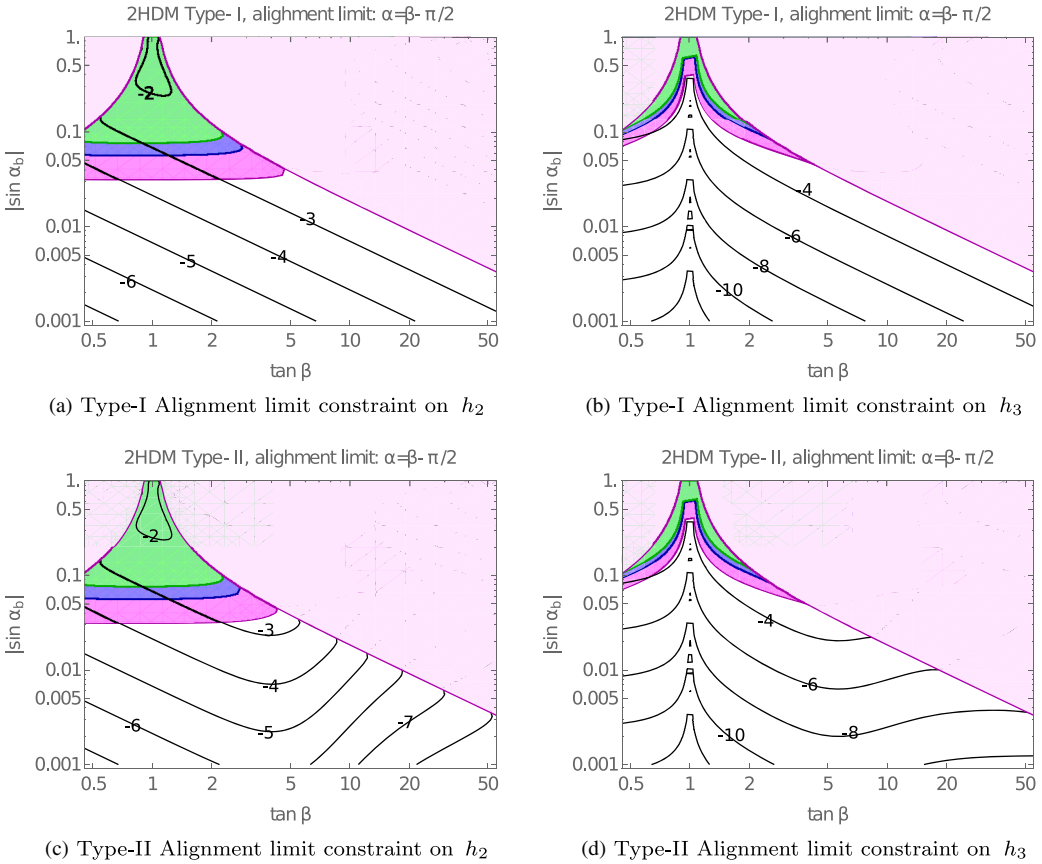

(a) Type-I Alignment limit constraint on h_2

(b) Type-I Alignment limit constraint on h_3

(c) Type-II Alignment limit constraint on h_2

(d) Type-II Alignment limit constraint on h_3

FIG. 3. Exclusion limits for the heavy Higgs resonant productions in the alignment limit with $m_{h_2} = 550$ GeV, $m_{h_3} = 600$ GeV, $m_{H^\pm} = 620$ GeV, $\nu = 1$. The plots in the first and second row represent the constraints for the Type-I and Type-II models, respectively. The left (right) column shows the constraints from the resonant production of $h_2(h_3)$. The pink region is theoretically inaccessible as described in the text. The green, blue, and magenta regions represent the exclusion limits for the LHC integrated luminosities equal to 100 fb^{-1}, 300 fb^{-1} and 3000 fb^{-1}, respectively. The black contour represents the logarithm of $\log \overline{|M|_i^2}$ in Eq. (39) with $s = m_{h_{2,3}}$ for $i = 2, 3$.

We now consider the prospective future reach at the LHC. In the alignment limit, the sensitivity comes primarily from the resonant production of h_2, as expected from Eqs. (29) and (30). We show the prospective exclusion regions associated with $h_{2,3}$ production separately in Fig. 3. The pink region is forbidden by the requirement of the electroweak symmetry breaking. The green, blue, and magenta regions represent the prospective exclusion limits for the LHC integrated luminosities equal to 100 fb^{-1}, 300 fb^{-1} and 3000 fb^{-1}, respectively. The black contours correspond to $\log_{10}\overline{|M|_i^2}$ in Eq. (39) with $s = m_{h_{2,3}}$ for $i = 2, 3$. If we require $\overline{|M|_i^2} > 10^{-4}$ to guarantee the dominance of the resonant production, then there will be some parts of the prospective exclusion region for 3000 fb^{-1} at low $\tan\beta$ that may not be valid for our analysis. One could observe that from Fig. 6(b) and Fig. 6(d) there is a loss of sensitivity for h_3 near $\tan\beta \approx 1$ in the alignment limit for both Type-I and Type-II models. This is due to the cancellation effect in the coupling g_{3z1} when $-\alpha = \beta = \pi/4$.

The situation is similar for nonvanishing but small θ. An illustration for $\cos(\beta - \alpha) = 0.02$ is shown in Fig. 4. However, for a large deviation, for example $\cos(\beta - \alpha) = 0.05$ in the Type-II model and $\cos(\beta - \alpha) = 0.1$ in the Type-I model, the constraints from the resonance production of h_3 become important, and can cover large part of the parameter space. In this situation, the effect of the nonresonant production is negligible due to a relatively large $\overline{|M|_3^2}$. This can be seen in Fig. 5.

In Fig. 6, we show the corresponding separate exclusion limit for $m_{h_2} = 400$ GeV and $m_{h_3} = 450$ GeV and contours for $\log \overline{|M|_i^2}$. Compare with Fig. 3 we find that the values of $\overline{|M_i|^2}$ at $s = m_{h_i}^2$ are larger than those of heavier Higgs mass. In other words, the peak in the distribution of the invariant mass of final state particles is more prominent for smaller heavy Higgs mass and the interference effects are rather small. Hence, all the exclusion regions we derive satisfy the requirement $\overline{|M|_i^2} > 10^{-4}$.

In addition, we take into account the constraint from the Higgs coupling measurements at 7 and 8 TeV LHC as what

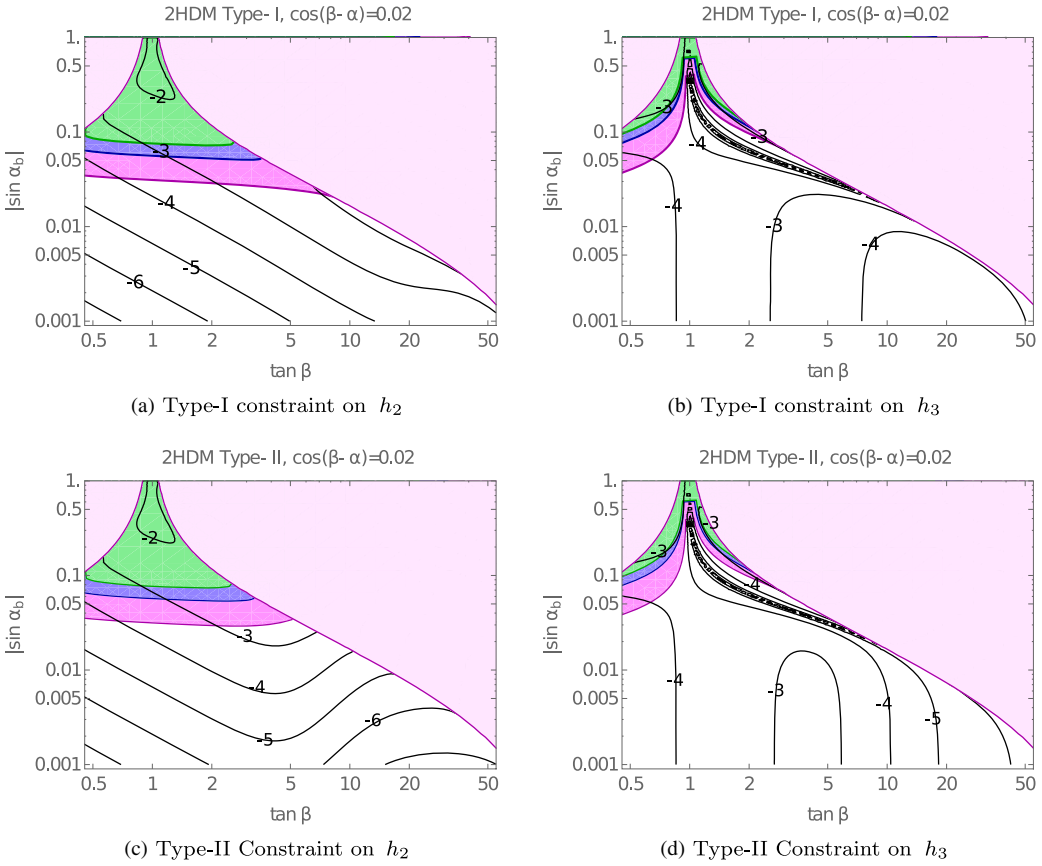

(a) Type-I constraint on h_2 (b) Type-I constraint on h_3

(c) Type-II Constraint on h_2 (d) Type-II Constraint on h_3

FIG. 4. Exclusion limits for the heavy Higgs resonant productions in the Type-I and Type-II 2HDMs with $\cos(\beta-\alpha)=0.02$, $m_{h_2}=550$ GeV, $m_{h_3}=600$ GeV, $m_{H^\pm}=620$ GeV, $\nu=1$. The plots in the first and second row represent the constraints for the Type-I and Type-II models, respectively. The left (right) column shows the constraints from the resonance production of $h_2(h_3)$. The pink region is theory-inaccessible. The green, blue, and magenta regions represent the exclusion limits for the LHC integrated luminosities equal to 100 fb^{-1}, 300 fb^{-1} and 3000 fb^{-1}, respectively. The black contour represents the logarithm of $\log\overline{|M|_i^2}$ in Eq. (39) with $s=m_{h_{2,3}}$ for $i=2,3$.

was done in Ref. [24]. The channels included in the χ^2 analysis are: $h_1\to WW, ZZ, \gamma\gamma, bb, \tau\tau$. We also include the present and prospective constraints from EDM searches given in Ref. [19], which are summarized in Table VIII. We find that the constraints from LHC and low energy experiments are complementary. Figures 7 and 8 demonstrate the exclusion limits from both LHC and EDM searches. In each figure, the orange region gives the current LHC exclusion limit. The blue and magenta regions represent prospective future LHC limits for integrated luminosities equal to 300 fb^{-1} and 3000 fb^{-1}, respectively. The light green and light blue regions are excluded by the neutron EDM and electron EDM searches, respectively. The light red and light yellow represents current constraints from the mercury and prospective radium atomic EDM searches. The gray regions are excluded by the Higgs coupling measurements. The pink region is again as described above theory-inaccessible. There are also constraints that we do not show in Fig. 7 and Fig. 8 from heavy flavor physics [47], which exclude the regions of parameter space with $\tan\beta$ less than 0.9 in both Type-I and Type-II models for the benchmark point we choose. These constraints can be relaxed if other new particles are introduced in addition to the 2HDMs or some nontrivial flavor structure [48,49]. Figure 3 of Ref. [47] demonstrates the constraints on the $\tan\beta$ vs m_{H^+} plane for the Type-I and Type-II 2HDMs. The most stringent bounds on $\tan\beta$ come from $B_s-\bar{B}_s$ mixing and $B_s^0\to\mu^+\mu^-$ for the Type-I model, and from $B_s-\bar{B}_s$ and $B_d-\bar{B}_d$ mixing for the Type-II model.

In Figs. 7(a) and 7(b), we show the current and prospective exclusion regions for the Type-I model in the alignment limit. One can see that the reach of the collider search is not competitive with that of the electron EDM search even at the end of the HL-LHC phase, especially in the low $\tan\beta$ region. This is due to the fact that the collider search is sensitive to $\mathrm{Br}(h_{2,3}\to Zh_1)$ in addition to the $h_{2,3}$ production cross sections. In the alignment limit, the Zh_1 channel is fed mainly from the decay of h_2, and the coupling g_{2z1} is suppressed by the CPV angle α_b as shown in Eq. (29). Moreover, for low $\tan\beta$, the

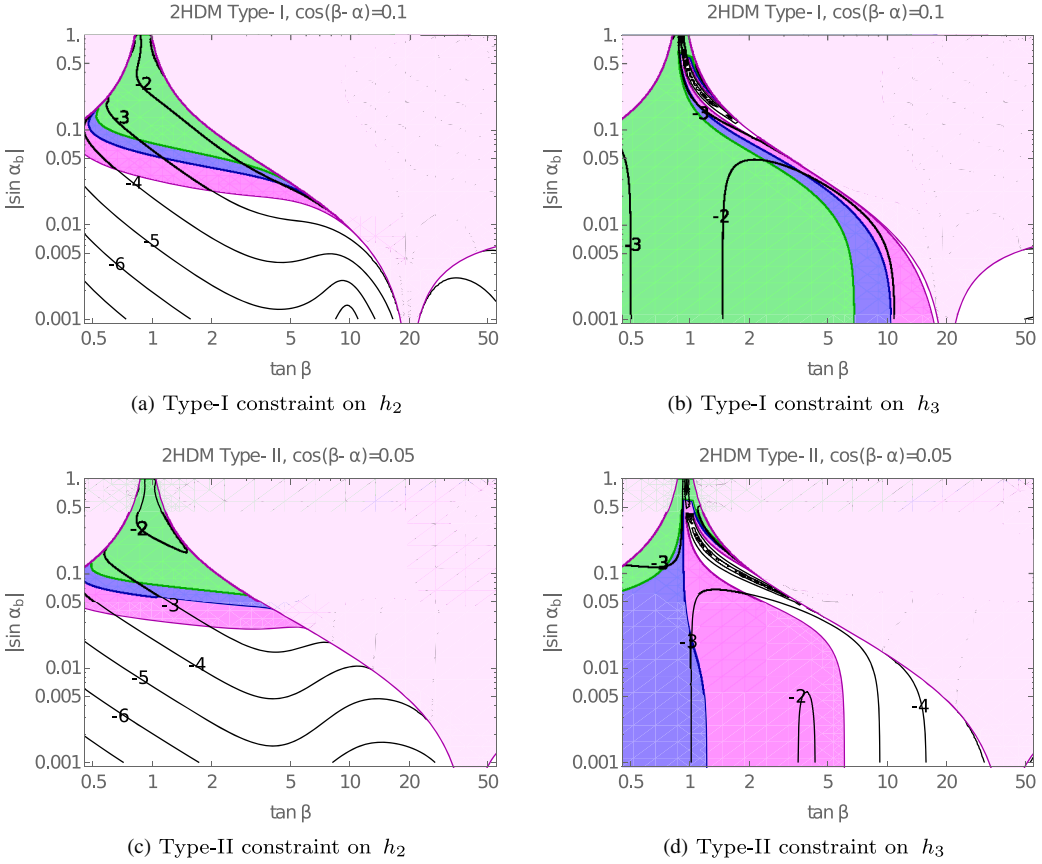

(a) Type-I constraint on h_2 (b) Type-I constraint on h_3

(c) Type-II constraint on h_2 (d) Type-II constraint on h_3

FIG. 5. Exclusion limits for the heavy Higgs resonant productions with $m_{h_2} = 550$ GeV, $m_{h_3} = 600$ GeV, $m_{H^\pm} = 620$ GeV, $\nu = 1$, and $\cos(\beta - \alpha) = 0.1$ (Type-I), $\cos(\beta - \alpha) = 0.05$ (Type-II). The plots in the first and second row represent the constraints for the Type-I and Type-II models, respectively. The left (right) column shows the constraints from the resonance production of $h_2(h_3)$. The pink region is theoretically inaccessible. The green, blue, and magenta regions represent the exclusion limits for the LHC integrated luminosities equal to 100 fb^{-1}, 300 fb^{-1} and 3000 fb^{-1}, respectively. The black contour represents the logarithm of $\log \overline{|M|_i^2}$ in Eq. (39) with $s = m_{h_{2,3}}^2$ for $i = 2, 3$.

couplings of h_2 to quarks are enhanced, which leads to a suppression on $\mathrm{Br}(h_2 \to Zh_1)$ and an increasing gluon fusion h_2 production cross section. However, the increase of the latter cannot compensate for the decreasing $\mathrm{Br}(h_2 \to Zh_1)$. The net effect is a reduced Zh_1 signal strength. In contrast, the electron EDM is sensitive to the pseudoscalar couplings that are enhanced at low $\tan\beta$ in the Type-I model, so electron EDM searches exclude a large part of parameter space in the low $\tan\beta$ region in Fig. 7(b).

In Figs. 7(c) to 7(f), we present the current and prospective exclusion regions away from the alignment limit. We can observe that the current collider constraints are not as strong as those from EDMs. However, the future LHC reach can be comparable to that of the EDMs searches, and even better at moderate $\tan\beta$. One can observe this feature from Eq. (30), where g_{3z1} is proportional to θ which describes the level of deviation from the alignment limit, in contrast to Eq. (29) where g_{2z1} is suppressed by the small CPV angle α_b. One can also observe that in the large $\tan\beta$ region the LHC loses sensitivity. The reason is that at large $\tan\beta$, pseudoscalar couplings of both t and b quarks to h_3 are suppressed, so the total partonic production cross section $\hat{\sigma}(gg \to h_3)$ decreases as $\tan\beta$ increases. Despite the possible increase in $\mathrm{Br}(h_3 \to Zh_1)$, the over all effect is a decreasing trend of signal rate towards large $\tan\beta$ resulting in an untestable region for the LHC search.

In the Type-II model, the results are shown in Fig. 8. In contrast to the Type-I model, the electron and mercury EDMs are not able to probe the parameter space when $\tan\beta$ is close to one due to the cancellation in Barr-Zee diagrams indicated in [19,23], whereas the neutron and radium EDMs retain sensitivity in this region. In the situation that is close to the alignment limit, as one can observe from Fig. 8(a) to 8(d), the future LHC reach can help to test the region where $\tan\beta$ is close to one. However, the reach of future neutron and radium EDM constraints still exceeds that of the LHC. When the deviation from the alignment limit is as large as $\cos(\beta - \alpha) = 0.05$, the future LHC may probe a large portion of the parameter space for reasons

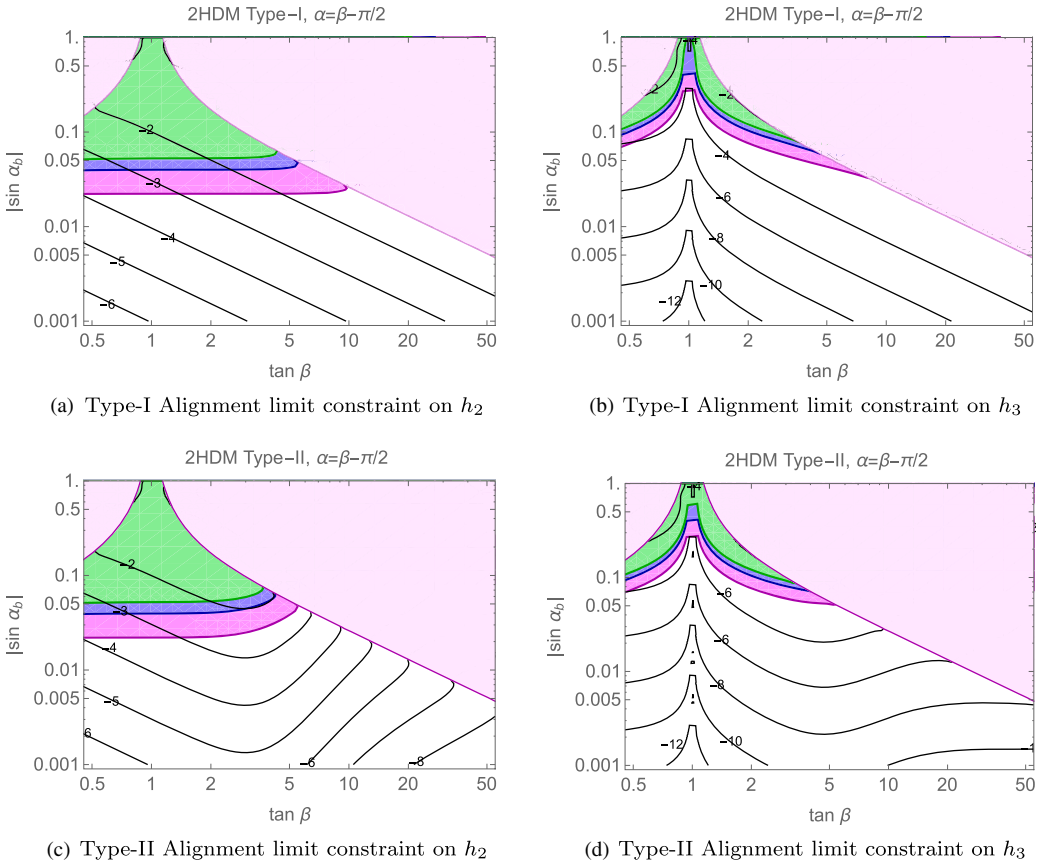

(a) Type-I Alignment limit constraint on h_2

(b) Type-I Alignment limit constraint on h_3

(c) Type-II Alignment limit constraint on h_2

(d) Type-II Alignment limit constraint on h_3

FIG. 6. Exclusion limits for the heavy Higgs resonant productions in the alignment limit $m_{h_2} = 400$ GeV, $m_{h_3} = 450$ GeV, $m_{H^\pm} = 420$ GeV, $\nu = 1$. The plots in the first and second row represent the constraints for the Type-I and Type-II models, respectively. The left (right) column shows the constraints from the resonant production of $h_2(h_3)$. The pink region is theoretically inaccessible as described in the text. The green, blue, and magenta regions represent the exclusion limits for the LHC integrated luminosities equal to 100 fb^{-1}, 300 fb^{-1} and 3000 fb^{-1}, respectively. The black contour represents the logarithm of $\log \overline{|M|}_i^2$ in Eq. (39) with $s = m_{h_{2,3}}^2$ for $i = 2, 3$.

similar to those for the Type-I model: g_{3z1} is sensitive to this deviation and is not suppressed by the CPV angle. Moreover, some portions of the large $\tan\beta$ region cannot be accessed, but for reasons different from the Type-I case. In the Type-II model, the pseudoscalar coupling of the t-quark to h_3 is suppressed at large $\tan\beta$, while the pseudoscalar coupling of the b-quark to h_3 is enhanced. However, for the range of $\tan\beta$ we are interested in, the enhancement of the b-quark loop contribution to $\hat{\sigma}(gg \to h_3)$ cannot compensate for the suppression of the t-quark loop effect as one can see from Fig. 10(d). Thus, $\hat{\sigma}(gg \to h_3)$ decreases with increasing $\tan\beta$. As for $\mathrm{Br}(h_3 \to Zh_1)$, due to the increasing $\mathrm{Br}(h_3 \to \bar{b}b)$ and decreasing $\mathrm{Br}(h_3 \to \bar{t}t)$, the overall effect leads to a decreasing $\mathrm{Br}(h_3 \to Zh_1)$. A decreasing production cross section combined with a decreasing decay branching ratio

TABLE VIII. Current and projected EDM constraints in units of e-cm. For the projected limits we assume that the sensitivity of nEDM is improved by two orders of magnitude, and eEDM is improved by one order of magnitude. The mercury EDM remains the same while future projected sensitivity of the radium EDM is assumed to be $d_{\mathrm{Ra}} < 10^{-27}$ e-cm.

Source	Current EDM (e-cm)	Projected EDM (e-cm)
Electron (e)	$d_{\mathrm{e}} < 8.7 \times 10^{-29}$ at 90% CL[15]	$d_{\mathrm{e}} < 8.7 \times 10^{-30}$ [18]
Neutron (n)	$d_{\mathrm{n}} < 2.9 \times 10^{-26}$ at 90% CL[16]	$d_{\mathrm{n}} < 2.9 \times 10^{-28}$ [18]
Mercury (Hg)	$d_{\mathrm{Hg}} < 7.4 \times 10^{-30}$ at 95% CL[50]	⋯
Radium (Ra)	⋯	$d_{\mathrm{Ra}} < 10^{-27}$ [18]

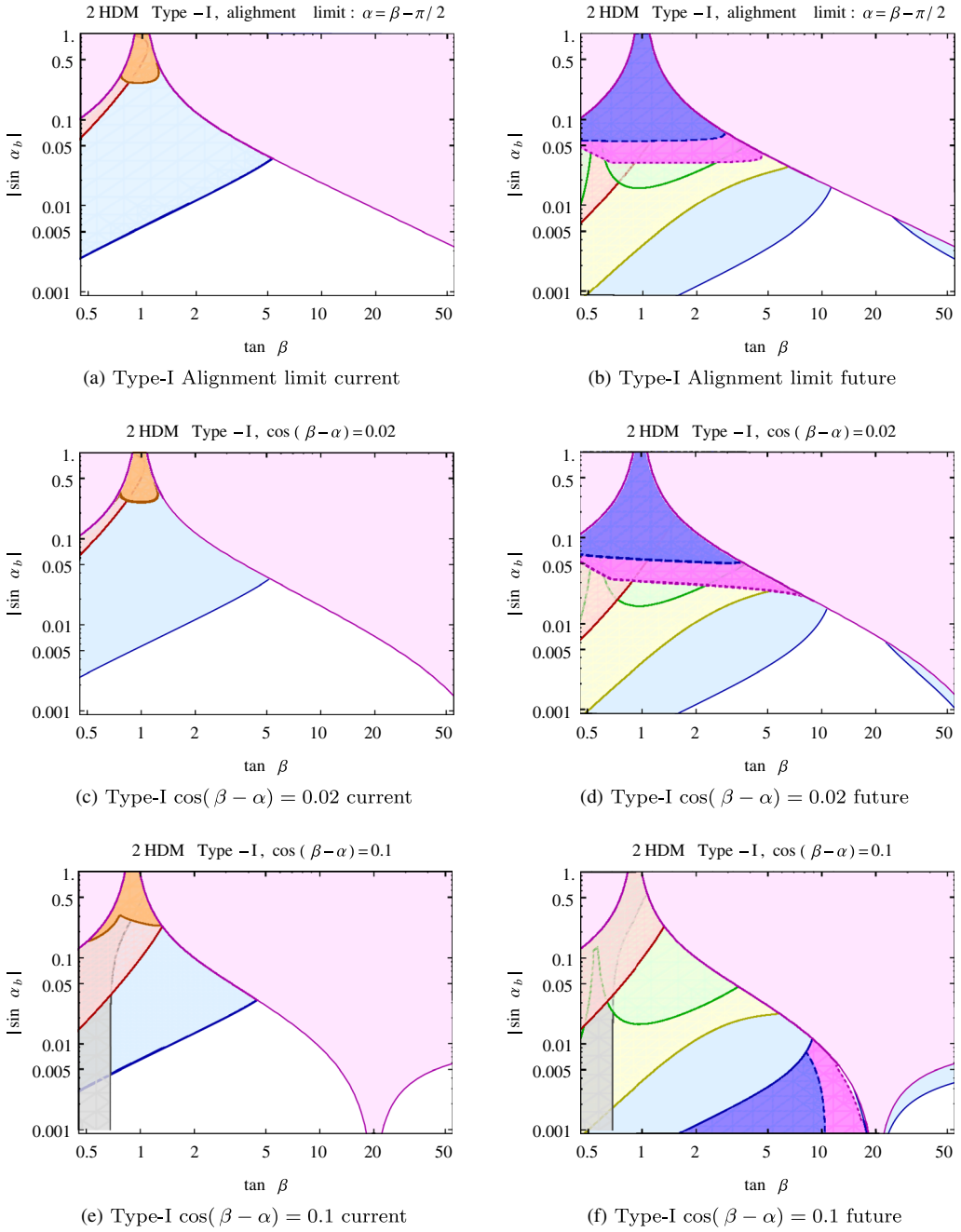

(a) Type-I Alignment limit current

(b) Type-I Alignment limit future

(c) Type-I $\cos(\beta-\alpha)=0.02$ current

(d) Type-I $\cos(\beta-\alpha)=0.02$ future

(e) Type-I $\cos(\beta-\alpha)=0.1$ current

(f) Type-I $\cos(\beta-\alpha)=0.1$ future

FIG. 7. Exclusion regions for the collider and EDM experiments in the Type-I 2HDM. The left (right) column is for the current (future) exclusion limit. The orange region is excluded by the current LHC data. The blue and magenta regions represent the future LHC limit with integrated luminosities equal to 300 fb^{-1} and 3000 fb^{-1}, respectively. Light transparent red represents the constraint from mercury EDM, light blue denotes electron EDM, light transparent green stands for neutron EDM, and light yellow signifies future prospective radium EDM. The gray region is excluded by the coupling measurement of the SM-like Higgs and the pink region is theoretically inaccessible due to the absence of a real solution for α_c. The benchmark point used here is $m_{h_2}=550$ GeV, $m_{h_3}=600$ GeV, $m_{H^\pm}=620$ GeV, $\nu=1$.

makes the large $\tan\beta$ region relatively inaccessible for the LHC in the Type-II model.

To show the influence of the overall mass scale on the exclusion regions, we present the current and future prospective exclusion limits for both Type-I and Type-II models in the alignment limit in Fig 9. Comparing Fig. 9(a) and 9(b) with Fig. 7(a) and Fig. 7(b), one finds that for the lighter mass benchmark point the exclusion region is generally larger than that of heavier mass point. The reason is that for lighter mass point the resonant production cross

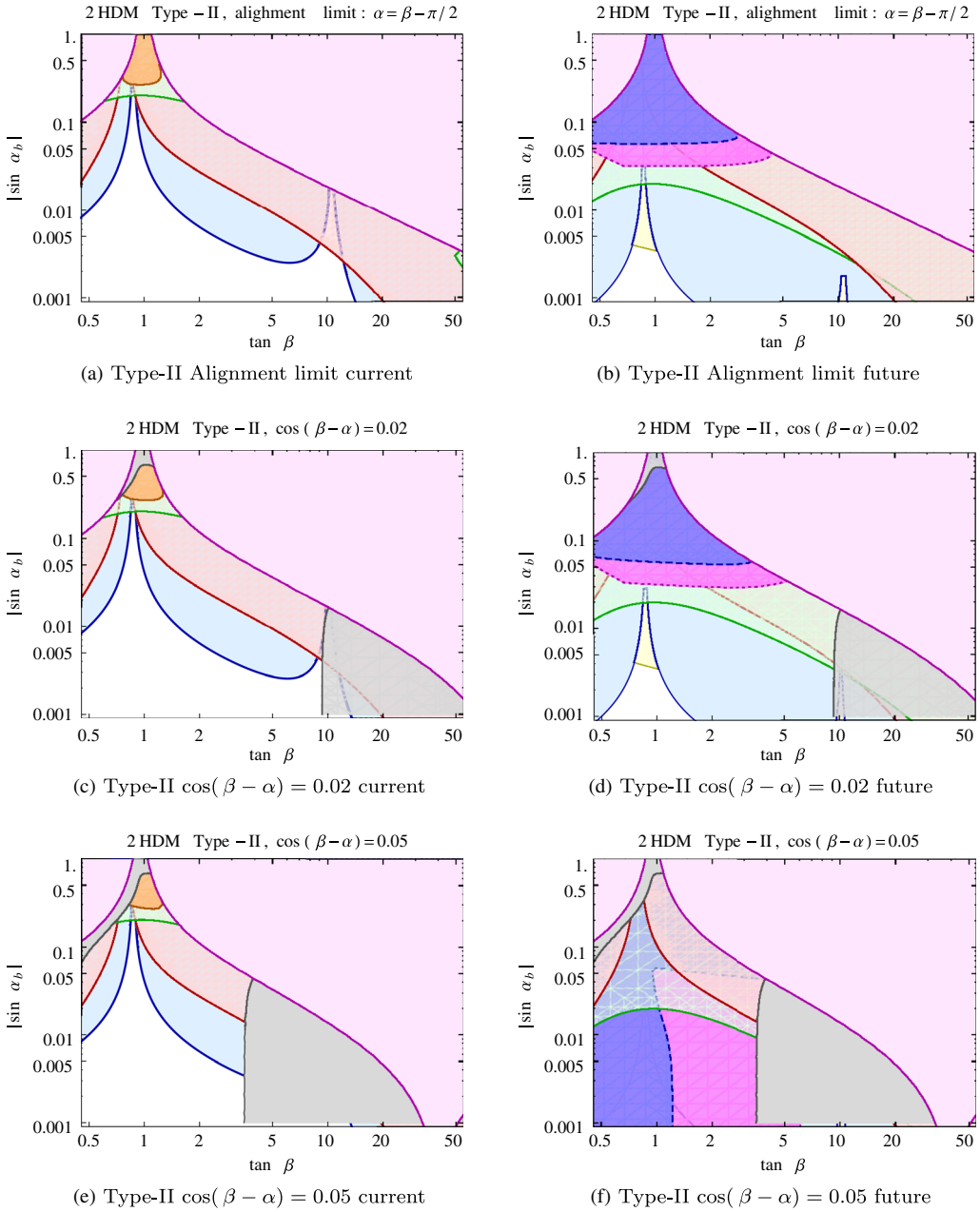

(a) Type-II Alignment limit current

(b) Type-II Alignment limit future

(c) Type-II $\cos(\beta-\alpha)=0.02$ current

(d) Type-II $\cos(\beta-\alpha)=0.02$ future

(e) Type-II $\cos(\beta-\alpha)=0.05$ current

(f) Type-II $\cos(\beta-\alpha)=0.05$ future

FIG. 8. Exclusion regions for the collider and EDM experiments in the Type-II 2HDM. The left (right) column is for the current (future) exclusion limit. The orange region is excluded by the current LHC data. The blue and magenta regions represent the future LHC limit with integrated luminosities equal to 300 fb^{-1} and 3000 fb^{-1}, respectively. Light transparent red represents the constraint from mercury EDM, light blue denotes electron EDM, light transparent green stands for neutron EDM, and light yellow signifies future prospective radium EDM. The gray region is excluded by the coupling measurement of the SM-like Higgs and the pink region is theoretically inaccessible due to the absence of a real solution for α_c. The benchmark point used here is $m_{h_2}=550$ GeV, $m_{h_3}=600$ GeV, $m_{H^\pm}=620$ GeV, $\nu=1$.

sections for the heavy Higgses increase, so the signal rates are larger compared with those in the heavier mass case. Another feature for the lighter mass scale is that in the region with small $\tan\beta$, the future exclusions are not restricted by the interference effects as the peak value of the amplitude of the resonant process grows. A similar situation occurs for $\cos(\beta-\alpha)$ away from the alignment limit, though we do not show this explicitly. Larger exclusion regions are obtained for the lighter mass point with the same $|\sin\alpha_b|$, $\tan\beta$, and $\cos(\beta-\alpha)$.

Now we argue that the future result of EDM and LHC experiments are expected to be complementary to

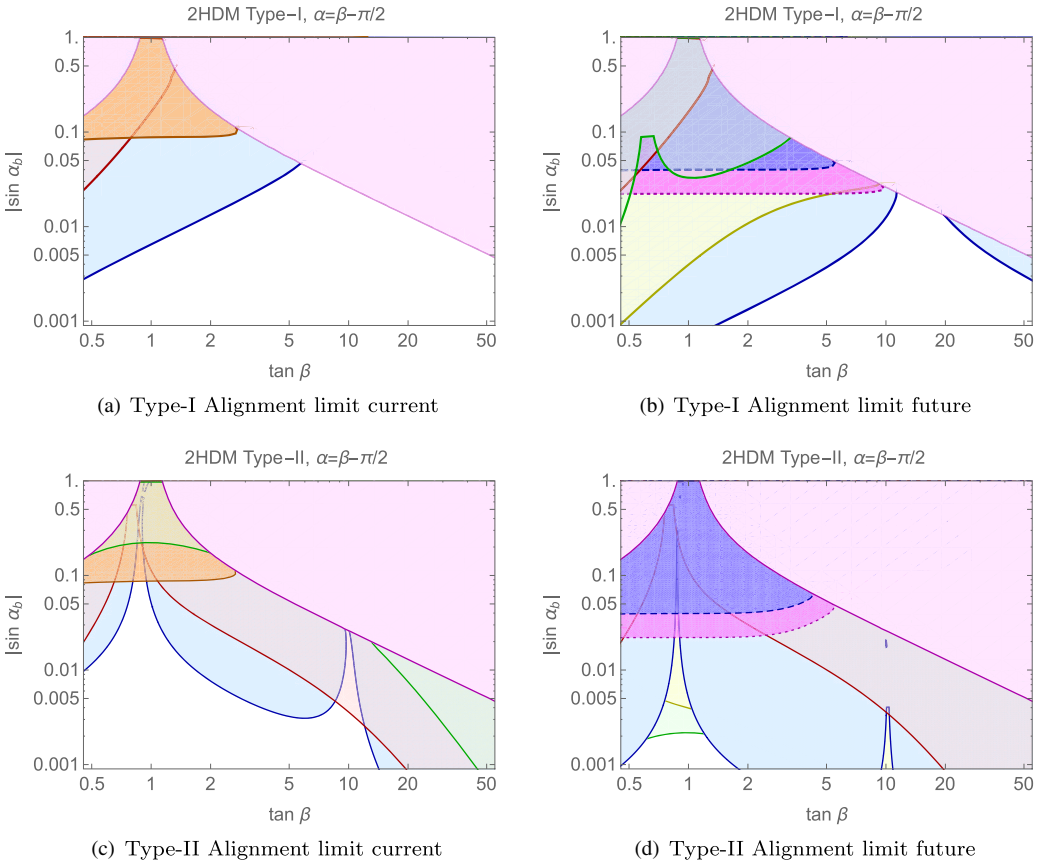

(a) Type-I Alignment limit current

(b) Type-I Alignment limit future

(c) Type-II Alignment limit current

(d) Type-II Alignment limit future

FIG. 9. Exclusion regions for the collider and EDM experiments in the Type-I and Type-II 2HDM with lighter Higgs mass hierarchy. The left (right) column is for the current (future) exclusion limit. The orange region is excluded by the current LHC data. The blue and magenta regions represent the future LHC limit with integrated luminosities equal to 300 fb^{-1} and 3000 fb^{-1}, respectively. Light transparent red represents the constraint from mercury EDM, light blue denotes electron EDM, light transparent green stands for neutron EDM, and light yellow signifies future prospective radium EDM. The gray region is excluded by the coupling measurement of the SM-like Higgs and the pink region is theoretically inaccessible due to the absence of a real solution for α_c. The benchmark point used here is $m_{h_2} = 400$ GeV, $m_{h_3} = 450$ GeV, $m_{H^\pm} = 420$ GeV, $\nu = 1$.

each other and combining information from two kinds of experiments would help us better determine if the 2HDMs are realized in the nature. Since the global fit of the Higgs coupling measurements constrains 2HDMs in the parameter space that are close to the alignment limit, we summarize our results in two categories: 2HDMs are in the exact alignment limit ($\cos(\beta-\alpha)=0$), 2HDMs deviate from the alignment limit (i.e. $\cos(\beta-\alpha)\neq 0$).

(1) 2HDMs in the alignment limit:

(a) *Future LHC makes a discovery*

As discussed above, in the alignment limit, the productions of the heavy Higgses h_2 and h_3 are purely determined by the size of CPV angle α_b, so the reach of future LHC is merely sensitive to the CPV effect in the model. From Fig. 7(b), one can observe that, in the Type-I model, the reach of future LHC is entirely inside the reach of future radium and electron EDM experiments. Thus, one can conclude that if Type-I model is true, with a discovery at the future LHC one should also observe nonzero radium and electron EDMs, otherwise the null results of radium and electron EDMs will veto the Type-I CPV 2HDM. A similar conclusion can be drawn for the Type-II model by observing Fig. 8(b), where one can find that the LHC sensitive region is well within the reaches of radium and neutron EDMs. Hence, if the Type-II model is true, the discovery of the future LHC should lead to the observations of nonzero radium and neutron EDMs.

(b) *Future LHC gives a null result*

For both Type-I and Type-II models, a null result from future LHC does not exclude the possibility of CPV in 2HDM as long as CPV angle α_b is sufficiently small. Meanwhile, any

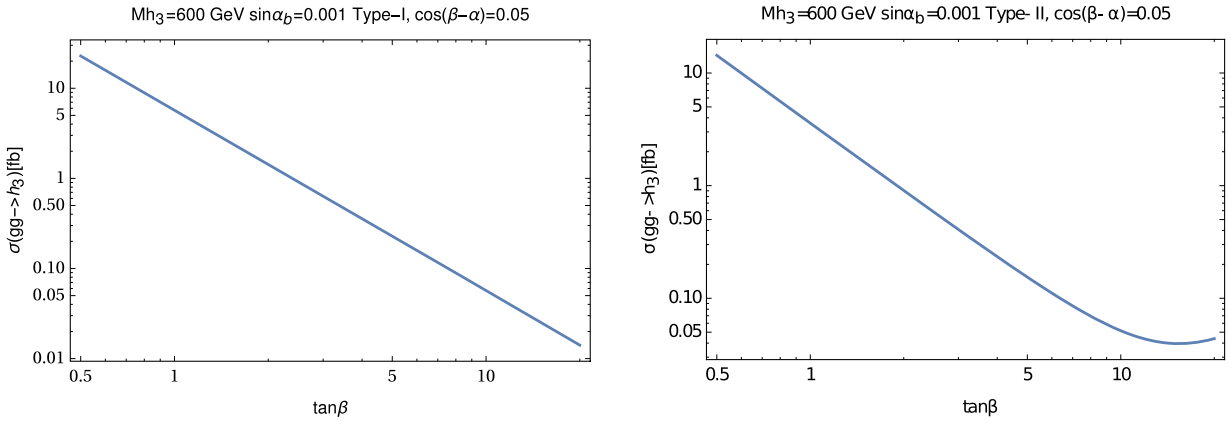

(a) Type-I production cross-section for h_3 (b) Type-II production cross-section for h_3

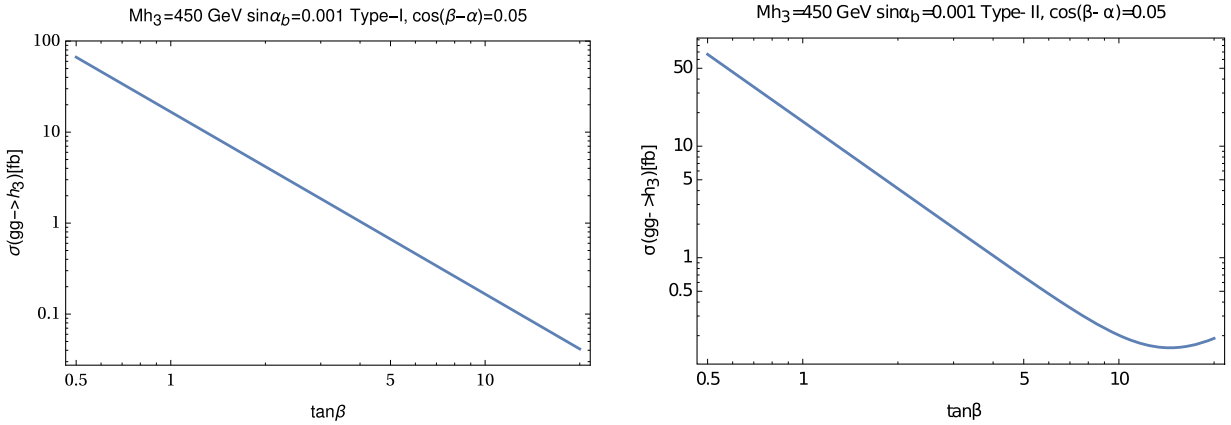

(c) Type-I production cross-section for h_3 (d) Type-II production cross-section for h_3

FIG. 10. Production cross section for h_3 for Type-I (left), Type-II (right) model.

nonzero EDMs that correspond to the regions of parameter space within the reach of LHC would disfavor the CPV 2HDMs.

(2) 2HDMs away from the alignment limit:

(a) *Future LHC makes a discovery*

In this case, the result from future LHC is not purely sensitive to the CPV effect since the coupling of h_3 to Zh_1 is proportional to the level of deviation from the alignment limit and is not suppressed by the CPV angle α_b. A discovery at the future LHC may or may not imply a nonzero EDM result, a situation that depends largely on the magnitude of deviation from the alignment limit. Moreover, if the deviation is relatively small, such as $\cos(\beta-\alpha)=0.02$, the exclusion limit would mainly come from h_2, for which production is purely sensitive to the CPV angle α_b, as shown in Fig. 7(d) and Fig. 8(d) for the Type-I and Type-II models, respectively. In addition, one would expect the nonzero radium and electron EDMs for the Type-I model and nonzero radium and neutron EDMs for the Type-II model. Thus, a null EDM result would disfavor both Type-I and Type-II CPV 2HDMs. On the other hand, if the deviation is relatively large, such as $\cos(\beta-\alpha)=0.1$ in the Type-I model [Fig. 7(f)] and $\cos(\beta-\alpha)=0.05$ in the Type-II model [Fig. 8(f)], the exclusion power would be dominated by the h_3 decay. As mentioned above, the discovery of h_3 does not necessarily lead to sizable EDMs, and therefore a more detailed study of the *CP* properties of the newly discovered particle would be needed.

(b) *Future LHC gives a null result*

In this case, for sufficiently large deviations as shown in Fig. 7(f) and Fig. 8(f), the discovery of any EDM results would indicate that the CPV source is not consistent with the CPV 2HDMs. On the other hand, for relatively a small deviation as shown in Fig. 7(d) and Fig. 8(d), the CPV 2HDMs is still available if CPV angle α_b is sufficiently small. Moreover, any nonzero

EDMs that correspond to the regions of parameter space within the reach of LHC would disfavor the CPV 2HDMs.

Finally, we comment on the potential constraints from the viability of successful EWBG in 2HDMs. One can potentially include the allowed regions where EWBG is viable in Figs. 7 and 8. For example, the authors of Ref. [29] studied the CPV for EWBG and identified some regions of parameter space that seem favorable. They pointed out that the CP-violating phase necessary for successful baryogenesis is sensitive to $\tan\beta$ and the masses of the heavy Higgses. That work also concentrated on parameter space region where the dominant decay channel of h_3 is to the Zh_2 final state ($A \to ZH$ in the CP-conserving limit), based on earlier studies of the electroweak phase transition [10,51]. A strong first order electroweak phase transition favors—but does not absolutely require—regions of parameter space leading to dominance of this decay mode. In this paper our main focus is on constraints of the CP-violating phases from the LHC and EDMs in 2HDMs. It is possible that for the spectra considered here, the CPV 2HDMs can accommodate a strong first order electroweak phase transition and give rise to the CPV asymmetries needed for successful baryogenesis. A detailed and general analysis of this possibility is beyond the scope of the present paper and will be left for future study.

VI. CONCLUSIONS

The CP properties of the SM-like Higgs boson provide a portal to investigate the possibility of CP-violation beyond the Standard Model, an important ingredient for successful baryogenesis. A CP-violating 2HDM with an approximate Z_2 symmetry may provide this source of CP-violation. Future searches for new scalars arising in the 2HDM, together with next generation EDM searches, may both discover the 2HDM and determine whether or not it contains the CPV interactions necessary for electroweak baryogenesis. In this paper, we have studied how well a future LHC search for a heavy Higgs with Zh_1 decay mode and $Z(\ell\ell)h_1(bb)$ final state can probe the parameter space of CP-violating 2HDMs. We used the BDT method to estimate the future exclusion limits on the observable $\sigma(gg \to h_{2,3}) \times \mathrm{Br}(h_{2,3} \to Zh_1) \times \mathrm{Br}(h_1 \to b\bar{b})$. We then compared this reach with that of next generation searches for the EDMs of the electron, neutron and neutral atoms.

Our results in Figs. 7 and 8, lead to the following conclusions: (1) In the exact alignment limit, a discovery at the LHC would imply observable radium and electron EDMs for the Type-I model and observable radium and neutron EDMs for the Type-II model. Null LHC results would still be consistent with CPV 2HDMs if the CPV angle is sufficiently small, but would not preclude observable EDMs. (2) Away from the alignment limit, a discovery at the LHC may or may not imply nonzero EDM results, depending on the level of deviation from the alignment limit. If the deviation is small, the LHC reach is mainly dominated by the production of the mostly CP-even Higgs (h_2). In this case, one can reach the same conclusion as in the alignment limit for both Type-I and Type-II models. However, with a relatively larger deviation, an LHC discovery may not imply nonzero EDM results because the production of the mostly CP odd Higgs (h_3) is not purely sensitive to the variation of the CPV phases. In addition, the LHC reach would cover most of the parameter space that can also be probed by the EDM searches. As a consequence, a null LHC result, together with observation of the EDMs, would disfavor the CPV 2HDMs. Finally, we also point out that our analysis may break down in the small $\tan\beta$ and α_b regions, due to the non-negligible interference effect between the resonant and nonresonant productions of Zh_1 through the gluon fusion channel. We leave the detailed study of this effect for future work.

ACKNOWLEDGMENTS

We thank Yue Zhang for helpful discussions and Satoru Inoue providing the codes generating the atomic EDM constraint. We also thank Huaike Guo for helping check the model file for CPV2HDM in the initial stage of this work. The work of C.-Y. C is supported by NSERC, Canada. Research at the Perimeter Institute is supported in part by the Government of Canada through NSERC and by the Province of Ontario through MEDT. The work of H. Li and M. J. R. M was supported in part under U.S. Department of Energy Contract No. DE-SC0011095. M. J. R. M. is also grateful for the hospitality of the Department of Physics at the University of Arizona, where a portion of this work was completed.

APPENDIX A: DISTRIBUTIONS OF BDT INPUT VARIABLES

We demonstrate the distributions of BDT input variables after our primary cuts described in Sec. IV B.

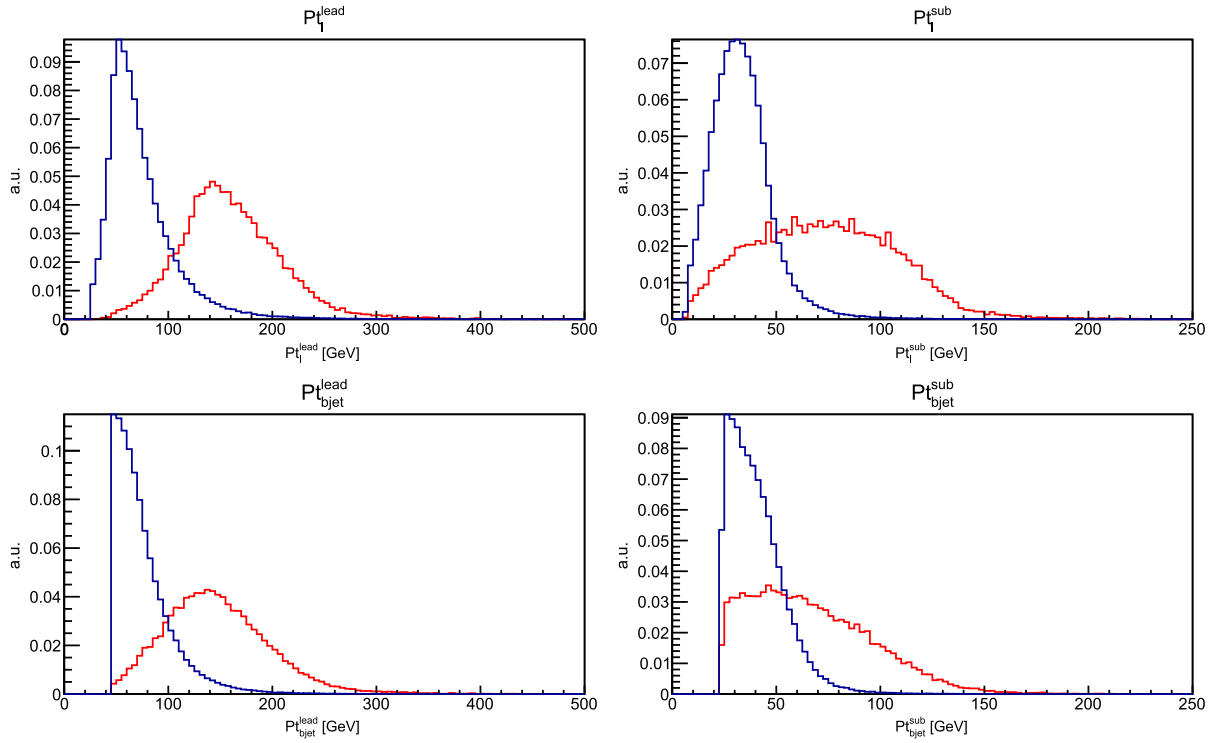

FIG. 11. Plots indicated by their titles showing the distributions of the lepton leading p_T, lepton subleading p_T, b-jet leading p_T, and b-jet subleading p_T, respectively. The units of the horizontal axes are GeV. The red histogram is for signal with heavy Higgs mass 550 GeV, and the blue histogram is for the combined background.

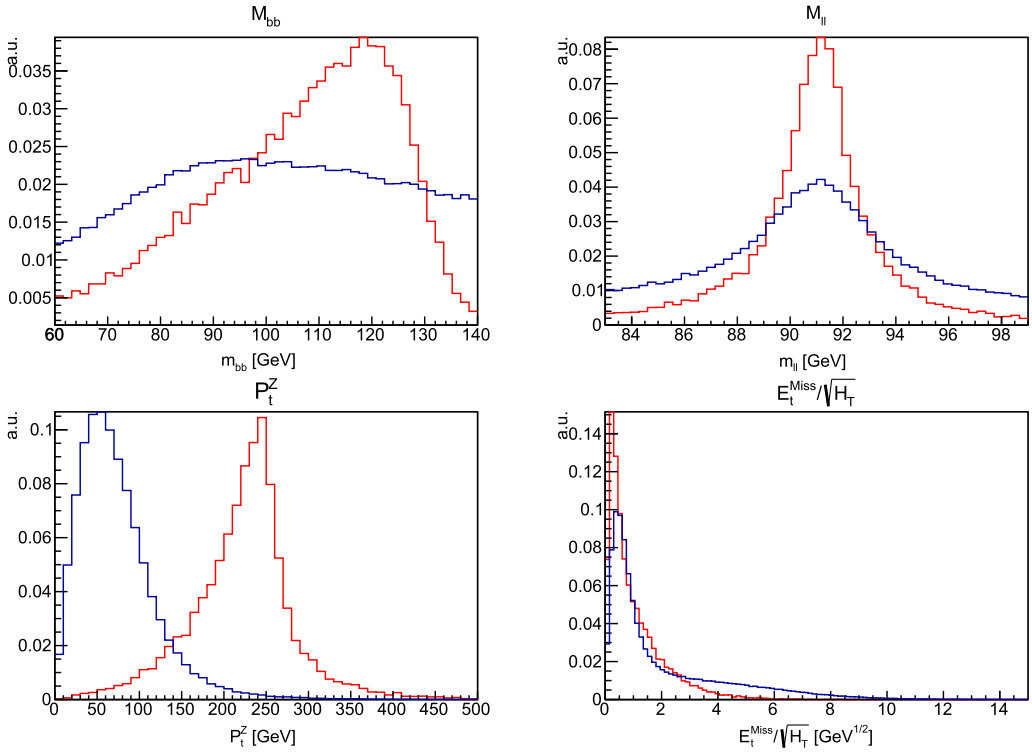

FIG. 12. Plots indicated by their titles showing the distributions of the reconstructed invariant mass for dijet system m_{bb}, reconstructed invariant mass for dilepton system m_{ll}, $E_T^{\text{miss}}/\sqrt{H_T}$, and reconstructed transverse momentum for Z boson p_T^Z, respectively. The units of the horizontal axes are GeV for m_{bb}, m_{ll}, p_T^Z, and $\text{GeV}^{1/2}$ for $E_T^{\text{miss}}/\sqrt{H_T}$. The red histogram is for the signal with heavy Higgs mass 550 GeV, and the blue histogram is for the combined background.

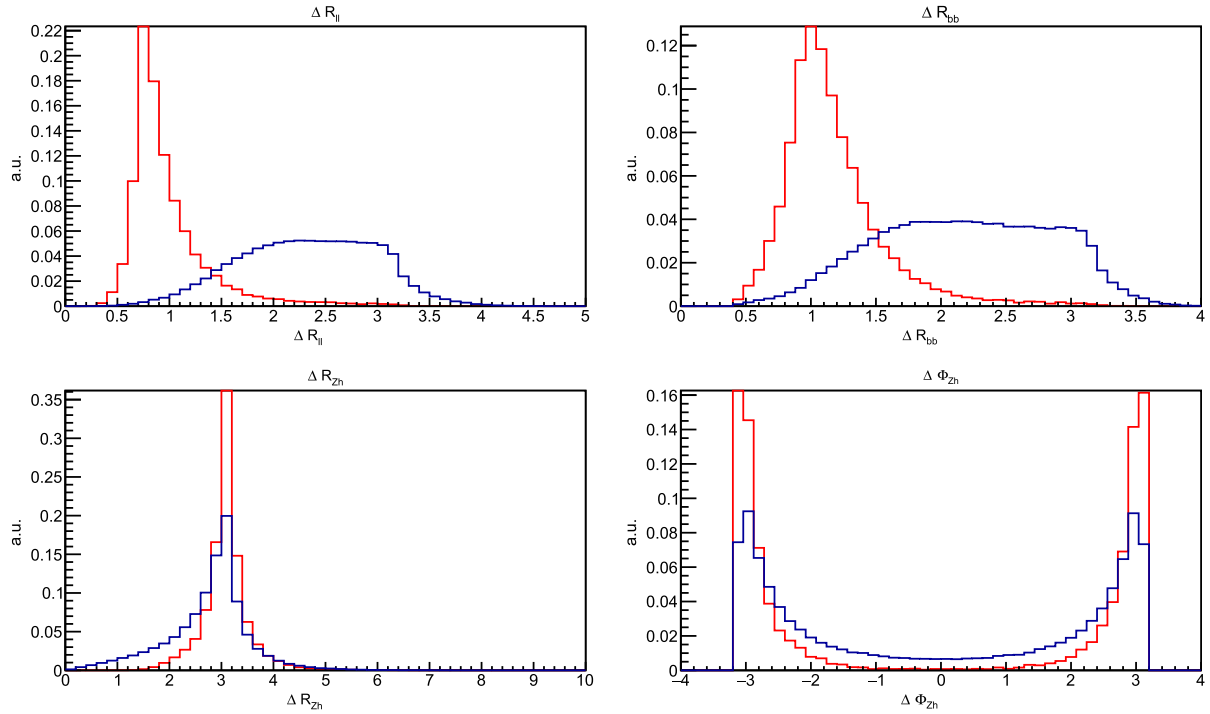

FIG. 13. Plots indicated by their titles showing the distributions of ΔR_{ll}, ΔR_{jj}, ΔR_{Zh} and $\Delta\Phi_{Zh}$, respectively. The red histogram is for signal with heavy Higgs mass 550 GeV, and the blue histogram is for the combined background.

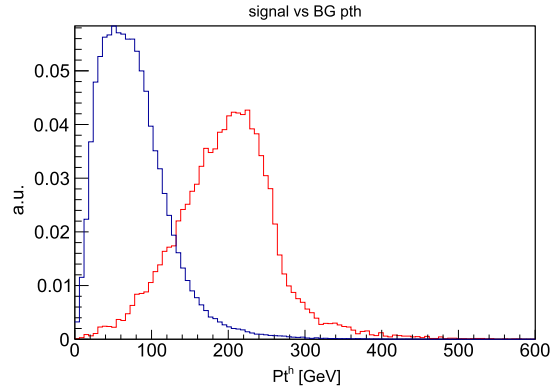

FIG. 14. Reconstructed transverse momentum for Higgs p_t^h, the unit of the horizontal axis is GeV. The red histogram is for signal with heavy Higgs mass 550 GeV; the blue histogram is for the combined background.

APPENDIX B: ANALYTICAL FORMULAS FOR HIGGS TWO-BODY DECAYS

Higgs two-body decay rates are listed in the following:

(i) $h_i \to gg$, heavy Higgs decays to two gluons

$$\Gamma(h_i \to gg) = \frac{\alpha_s^2 G_F m_{h_i}^3}{64\sqrt{2}\pi^3}[|c_{t,i}F_{1/2}^H(\tau_t^i) + c_{b,i}F_{1/2}^H(\tau_b^i)|^2 + |\tilde{c}_{t,i}F_{1/2}^A(\tau_t^i) + \tilde{c}_b^i F_{1/2}^A(\tau_b^i)|^2], \quad \text{(B1)}$$

where the functions $F_{1/2}^H$ and $F_{1/2}^A$ and the variable τ_f^i are defined in Eqs. (33) to (34).

(ii) $h_i \to Zh_1$, heavy Higgs decays to Z boson and SM-like Higgs

$$\Gamma(h_i \to Zh_1) = \frac{|g_{iz1}|^2}{16\pi m_{h_i}^3}\sqrt{(m_{h_i}^2-(m_{h_1}+M_Z)^2)(m_{h_i}^2-(m_{h_1}-M_Z)^2)} \times \left[-(2m_{h_i}^2+2m_{h_1}^2-M_Z^2)+\frac{1}{M_Z^2}(m_{h_i}^2-m_{h_1}^2)^2\right], \quad \text{(B2)}$$

where g_{iz1} is defined in Eq. (28).

(iii) $h_i \to VV$, heavy Higgs decays to two vector bosons

$$\Gamma(h_i \to VV) = (a_i)^2\frac{G_F m_{h_i}^3}{16\sqrt{2}\pi}\delta_V\left(1-\frac{4M_V^2}{m_{h_i}^2}\right)^{1/2} \times \left[1-\frac{4M_V^2}{m_{h_i}^2}+\frac{3}{4}\left(\frac{4M_V^2}{m_{h_i}^2}\right)^2\right], \quad \text{(B3)}$$

where $V = W$, Z and $\delta_Z = 1$, $\delta_W = 2$, $i = 2, 3$.

(iv) $h_i \to f\bar{f}$, heavy Higgs decays to a fermion pair

$$\Gamma(h_i \to \bar{f}f) = [(c_{f,i})^2 + (\tilde{c}_{f,i})^2]\frac{N_c G_F m_f^2 m_{h_i}}{4\sqrt{2}\pi} \times \left(1 - \frac{4m_f^2}{m_{h_i}^2}\right)^{3/2}, \tag{B4}$$

where $N_c = 3$ for quarks, $N_c = 1$ for leptons.

(v) $h_i \to h_1 h_1$ heavy Higgs decays to a pair of SM Higgs

$$\Gamma(h_i \to h_1 h_1) = \frac{g_{i11}^2 v^2}{8\pi m_{h_i}}\sqrt{1 - \frac{4m_{h_1}^2}{m_{h_i}^2}}, \tag{B5}$$

where g_{i11} is defined by

$$g_{i11} = \left.\frac{\partial^3 V}{\partial h_i \partial h_1 \partial h_1}\right|_{H^\pm, h_i = 0}. \tag{B6}$$

[1] G. Aad *et al.* (ATLAS Collaboration), Phys. Lett. B **716**, 1 (2012).
[2] S. Chatrchyan *et al.* (CMS Collaboration), Phys. Lett. B **716**, 30 (2012).
[3] M. Trodden, Rev. Mod. Phys. **71**, 1463 (1999).
[4] J. M. Cline, arXiv:hep-ph/0609145.
[5] D. E. Morrissey and M. J. Ramsey-Musolf, New J. Phys. **14**, 125003 (2012).
[6] A. D. Sakharov, Pis'ma Zh. Eksp. Teor. Fiz. **5**, 32 (1967) [JETP Lett. **5**, 24 (1967)]; Usp. Fiz. Nauk **161**, 61 (1991) [Sov. Phys. Usp. **34**, 392 (1991)].
[7] K. Kajantie, M. Laine, K. Rummukainen, and M. E. Shaposhnikov, Phys. Rev. Lett. **77**, 2887 (1996).
[8] F. Csikor, Z. Fodor, and J. Heitger, Phys. Rev. Lett. **82**, 21 (1999).
[9] K. Rummukainen, M. Tsypin, K. Kajantie, M. Laine, and M. E. Shaposhnikov, Nucl. Phys. **B532**, 283 (1998).
[10] G. C. Dorsch, S. J. Huber, and J. M. No, J. High Energy Phys. 10 (2013) 029.
[11] L. Fromme, S. J. Huber, and M. Seniuch, J. High Energy Phys. 11 (2006) 038.
[12] J. M. Cline and P. A. Lemieux, Phys. Rev. D **55**, 3873 (1997).
[13] V. Khachatryan *et al.* (CMS Collaboration), Phys. Rev. D **92**, 012004 (2015).
[14] ATLAS Collaboration, Report No. ATLAS-CONF-2013-013.
[15] J. Baron *et al.* (ACME Collaboration), Science **343**, 269 (2014).
[16] C. A. Baker *et al.*, Phys. Rev. Lett. **97**, 131801 (2006).
[17] W. C. Griffith, M. D. Swallows, T. H. Loftus, M. V. Romalis, B. R. Heckel, and E. N. Fortson, Phys. Rev. Lett. **102**, 101601 (2009).
[18] K. Kumar, Z. T. Lu, and M. J. Ramsey-Musolf, arXiv: 1312.5416.
[19] S. Inoue, M. J. Ramsey-Musolf, and Y. Zhang, Phys. Rev. D **89**, 115023 (2014).
[20] J. Shu and Y. Zhang, Phys. Rev. Lett. **111**, 091801 (2013).
[21] M. Jung and A. Pich, J. High Energy Phys. 04 (2014) 076.
[22] N. Yamanaka, B. K. Sahoo, N. Yoshinaga, T. Sato, K. Asahi, and B. P. Das, Eur. Phys. J. A **53**, 54 (2017).
[23] L. Bian, T. Liu, and J. Shu, Phys. Rev. Lett. **115**, 021801 (2015).
[24] C. Y. Chen, S. Dawson, and Y. Zhang, J. High Energy Phys. 06 (2015) 056.
[25] L. Bian, N. Chen, and Y. Zhang, Phys. Rev. D **96**, 095008 (2017).
[26] A. G. Akeroyd *et al.*, Eur. Phys. J. C **77**, 276 (2017).
[27] N. Chen, J. Li, Y. Liu, and Z. Liu, Phys. Rev. D **91**, 075002 (2015).
[28] B. Coleppa, F. Kling, and S. Su, J. High Energy Phys. 09 (2014) 161.
[29] G. C. Dorsch, S. J. Huber, T. Konstandin, and J. M. No, J. Cosmol. Astropart. Phys. 05 (**2017**) 052.
[30] G. Aad *et al.* (ATLAS Collaboration), Phys. Lett. B **744**, 163 (2015).
[31] Y. Freund and R. E. Schapire, in *ICML'96 Proceedings of the Thirteenth International Conference on International Conference on Machine Learning* (Morgan Kaufmann, San Francisco, CA, 1996), p. 148.
[32] ATLAS Collaboration, Report No. ATLAS-CONF-2014-010.
[33] CMS Collaboration, Report No. CMS-PAS-HIG-16-007.
[34] S. L. Glashow and S. Weinberg, Phys. Rev. D **15**, 1958 (1977).
[35] V. D. Barger, J. L. Hewett, and R. J. N. Phillips, Phys. Rev. D **41**, 3421 (1990).
[36] G. C. Branco, P. M. Ferreira, L. Lavoura, M. N. Rebelo, M. Sher, and J. P. Silva, Phys. Rep. **516**, 1 (2012).
[37] https://twiki.cern.ch/twiki/bin/view/LHCPhysics/CrossSections.
[38] J. Alwall, R. Frederix, S. Frixione, V. Hirschi, F. Maltoni, O. Mattelaer, H.-S. Shao, T. Stelzer, P. Torrielli, and M. Zaro, J. High Energy Phys. 07 (**2014**) 079.
[39] T. Sjostrand, S. Mrenna, and P. Z. Skands, J. High Energy Phys. 05 (2006) 026.
[40] J. de Favereau, C. Delaere, P. Demin, A. Giammanco, V. Lemaître, A. Mertens, and M. Selvaggi (DELPHES 3 Collaboration), J. High Energy Phys. 02 (2014) 057.
[41] F. Febres Cordero, L. Reina, and D. Wackeroth, Phys. Rev. D **80**, 034015 (2009).

[42] M. Czakon, P. Fiedler, and A. Mitov, Phys. Rev. Lett. **110**, 252004 (2013).
[43] https://twiki.cern.ch/twiki/bin/view/LHCPhysics/LHCHXSWGWHZH.
[44] ATLAS Collaboration, Report No. ATLAS-CONF-2013-020.
[45] A. Hocker *et al.*, *Proc. Sci.*, ACAT2007 (2007) 040.
[46] B. Hespel, F. Maltoni, and E. Vryonidou, J. High Energy Phys. 06 (2015) 065.
[47] T. Enomoto and R. Watanabe, J. High Energy Phys. 05 (2016) 002.
[48] M. D. Campos, D. Cogollo, M. Lindner, T. Melo, F. S. Queiroz, and W. Rodejohann, J. High Energy Phys. 08 (2017) 092.
[49] A. Celis, M. Jung, X. Q. Li, and A. Pich, Phys. Lett. B **771**, 168 (2017).
[50] B. Graner, Y. Chen, E. G. Lindahl, and B. R. Heckel, Phys. Rev. Lett. **116**, 161601 (2016).
[51] G. C. Dorsch, S. J. Huber, K. Mimasu, and J. M. No, Phys. Rev. Lett. **113**, 211802 (2014).